JCI insight

CRISPR/Cas9 loss-of-function screen in a neuronal model of AP-4 deficiency identifies ATG9A trafficking modulators

Marvin Ziegler, Cedric Günter, Julian E. Alecu, Xutong Xue, Hyo-Min Kim, Afshin Saffari, Alexandra K. Davies, Mustafa Sahin, Darius Ebrahimi-Fakhari

JCI Insight. 2026. https://doi.org/10.1172/jci.insight.202204.

Resource and Technical Advance In-Press Preview **Cell biology** **Genetics** **Neuroscience**

Biallelic loss-of-function variants in the adaptor protein complex 4 (AP-4) disrupt trafficking of transmembrane proteins at the *trans*-Golgi network, including the autophagy-related protein 9A (ATG9A), leading to childhood-onset hereditary spastic paraplegia (AP-4-HSP). AP-4-HSP is characterized by features of both a neurodevelopmental and degenerative neurological disease. To investigate the molecular mechanisms underlying AP-4-HSP and identify potential therapeutic targets, we conducted an arrayed CRISPR/Cas9 loss-of-function screen of 8,478 genes, targeting the 'druggable genome', in a human neuronal model of AP-4 deficiency. Through this phenotypic screen and subsequent experiments, key modulators of ATG9A trafficking were identified, and complementary pathway analyses provided insights into the regulatory landscape of ATG9A transport. Knockdown of *ANPEP* and *NPM1* enhanced ATG9A availability outside the *trans*-Golgi network, suggesting they regulate ATG9A localization. These findings deepen our understanding of ATG9A trafficking in the context of AP-4 deficiency and offer a framework for the development of targeted interventions for AP-4-HSP.

CRISPR/Cas9 Loss-Of-Function Screen in a Neuronal Model of AP-4 Deficiency Identifies ATG9A Trafficking Modulators

Marvin Ziegler [1,2], Cedric Günter [1,3,#], Julian E. Alecu [1,#], Xutong Xue [1], Hyo-Min Kim [1], Afshin Saffari [1,4], Alexandra K. Davies [5,6], Mustafa Sahin [1,7], Darius Ebrahimi-Fakhari [1,8]

[1] Department of Neurology and F.M. Kirby Neurobiology Center, Boston Children's Hospital, Harvard Medical School, Boston, MA, 02115, USA

[2] Department of Functional Neuroanatomy, Institute of Anatomy and Cell Biology, Heidelberg University, 69120 Heidelberg, Germany

[3] Laboratory for Axon Growth and Regeneration, German Center for Neurodegenerative Diseases, 53127 Bonn, Germany

[4] Heidelberg University, Medical Faculty Heidelberg, University Hospital Heidelberg, Center for Pediatrics and Adolescent Medicine, Department of Pediatrics I, Division of Child Neurology and Metabolic Medicine, Heidelberg, Germany

[5] School of Biological Sciences, Faculty of Biology, Medicine and Health, Manchester Academic Health Science Centre, University of Manchester, Manchester, M13 9PT, UK

[6] Department of Proteomics and Signal Transduction, Max-Planck-Institute of Biochemistry, Martinsried, 82152, Germany

[7] Rosamund Stone Zander and Hansjoerg Wyss Translational Neuroscience Center, Boston Children's Hospital, Harvard Medical School, Boston, MA, 02115, USA

[8] Movement Disorders Program, Boston Children's Hospital, Harvard Medical School,

Boston, MA, 02115, USA

[#] These authors contributed equally.

Corresponding author:

Darius Ebrahimi-Fakhari, M.D., Ph.D., Movement Disorders Program, Department of Neurology, Boston Children's Hospital, CLSB 2nd floor, 3 Blackfan Circle, Boston, MA, 02115; Phone: +1 (617) 355-8356; darius.ebrahimi-fakhari@childrens.harvard.edu

DECLARATION OF INTERESTS

D.E.F. serves on the scientific advisory board (unpaid) for the following foundations: CureAP4 Foundation, The Maddie Foundation, SPG69/Warburg Micro Research Foundation, The Lilly & Blair Foundation, The Maurya Koduri Foundation, Genetic Cures for Kids Inc. D.E.F. received speaker honoraria from the International Parkinson and Movement Disorders Society and publishing royalties from Cambridge University Press. D.E.F. and M.S. hold the following patent: PCT/US2024/029856.

ABSTRACT

Biallelic loss-of-function variants in the adaptor protein complex 4 (AP-4) disrupt trafficking of transmembrane proteins at the *trans*-Golgi network, including the autophagy-related protein 9A (ATG9A), leading to childhood-onset hereditary spastic paraplegia (AP-4-HSP). AP-4-HSP is characterized by features of both a neurodevelopmental and degenerative neurological disease. To investigate the molecular mechanisms underlying AP-4-HSP and identify potential therapeutic targets, we conducted an arrayed CRISPR/Cas9 loss-of-function screen of 8,478 genes, targeting the 'druggable genome', in a human neuronal model of AP-4 deficiency. Through this phenotypic screen and subsequent experiments, key modulators of ATG9A trafficking were identified, and complementary pathway analyses provided insights into the regulatory landscape of ATG9A transport. Knockdown of *ANPEP* and *NPM1* enhanced ATG9A availability outside the *trans*-Golgi network, suggesting they regulate ATG9A localization. These findings deepen our understanding of ATG9A trafficking in the context of AP-4 deficiency and offer a framework for the development of targeted interventions for AP-4-HSP.

KEYWORDS

AP-4 deficiency syndrome, hereditary spastic paraplegia, ATG9A, functional genomics, high-content screening, CRISPR, autophagy, pathway analysis, protein trafficking, ANPEP, CD13

INTRODUCTION

Approximately one-third of all genes in the eukaryotic genome are predicted to encode transmembrane proteins that must traffic through various cellular compartments to function effectively (1,2). Defective transport of these proteins has been increasingly linked to a range of neurological diseases, including frontotemporal dementia, Charcot-Marie-Tooth disease, and several types of hereditary spastic paraplegia (HSP) (3,4). Among these, adaptor protein complex 4 (AP-4)-associated hereditary spastic paraplegia (AP-4-HSP) has emerged as a prototypical disorder of impaired protein trafficking. Clinically, AP-4-HSP manifests in early childhood with developmental delay / intellectual disability, progressive spasticity leading to loss of ambulation, epilepsy, secondary microcephaly, and developmental brain malformations (5–8). The condition arises from biallelic loss-of-function variants in one of four genes (*AP4B1*, *AP4E1*, *AP4M1*, *AP4S1*) encoding the subunits of the heterotetrameric AP-4 complex, which is critical for sorting cargo proteins from the *trans*-Golgi network (TGN) to early and late endosomes and pre-autophagosomal structures (PAS) (5,6).

Recent studies have identified ATG9A, the sole transmembrane protein in the autophagic machinery, as an important cargo of AP-4 (9–11). In AP-4-deficient cells, ATG9A accumulates in the TGN and is depleted from peripheral compartments. In neurons, this mislocalization leads to deficits in autophagy, impaired axon maintenance, and length-dependent axonal degeneration (11–16). However, residual autophagic activity and the presence of ATG9A outside the TGN suggest an alternative, AP-4-independent export

mechanism (9,11). This raises critical questions about how ATG9A trafficking is regulated in the context of AP-4 deficiency.

Genome-wide functional genomics screens have emerged as powerful tools to uncover regulators of cellular signaling. However, traditional approaches such as loss-of-function screening using small interfering RNA (siRNA) libraries are often limited by poor reproducibility due to inconsistent gene knockdown and off-target effects (17,18). Advances in CRISPR/Cas9-based gene interference, particularly its application in high-throughput screening assays, have addressed many of these limitations, ushering in a new era in functional genomics (19). While several large-scale CRISPR screens have been successfully conducted in recent years - primarily as pooled screens where cells are bulk transfected with a single guide RNA (sgRNA) library, selected for specific phenotypes, and analyzed using next-generation sequencing - these approaches pose significant challenges for assessing complex cellular phenotypes (20,21).

In contrast, arrayed CRISPR screens offer a microplate-based format in which gene modifications are performed individually in each well. This format eliminates the need for complex data deconvolution, facilitates the analysis of intricate readouts such as high-content microscopy, and leverages established platforms for siRNA and small molecule screening (19). Consequently, arrayed screens provide a robust and scalable approach for functional genomics with broad applications, including drug target discovery (22). However, only a limited number of arrayed CRISPR screens have been conducted to date (23–25).

Here, we present a large-scale CRISPR/Cas9 loss-of-function screen designed to identify modulators of ATG9A trafficking in a neuronal model of AP-4 deficiency, specifically targeting the ‘druggable genome’. By combining high-content imaging-based multiparametric analysis with a tailored pathway analysis for arrayed screening, we identify novel genes and pathways that modulate ATG9A trafficking. These findings reveal promising targets for drug development and open new avenues for therapeutic interventions in AP-4-HSP.

RESULTS

Establishing a Phenotypic High-Content Screen for Modulators of ATG9A Trafficking

We previously developed and validated a high-content imaging-based assay to measure intracellular ATG9A distribution as a surrogate for AP-4 function (26,27). To identify modulators of ATG9A trafficking in AP-4-deficient cells, we have now leveraged this assay to conduct an arrayed CRISPR/Cas9-based loss-of-function screen (*Fig. 1A*). Given that AP-4-HSP predominantly affects cortical and spinal neurons, we utilized the SH-SY5Y neuroblastoma cell line, which can be differentiated with retinoic acid into a neuron-like state resembling cholinergic neurons (28). For this study, we employed SH-SY5Y cells stably expressing wild-type Cas9, with and without expression of a sgRNA to knockout *AP4B1* (10). Western blot analysis confirmed Cas9 expression and the absence of AP4B1 protein in *AP4B1*^{KO} cells, which also displayed reduced levels of AP4E1, consistent with diminished overall AP-4 complex formation. As previously observed in other AP-4-deficient cells (9,10,14), ATG9A protein levels were elevated in *AP4B1*^{KO} cells (*Fig. 1B, S1)*.

For the CRISPR/Cas9-based loss-of-function screen, SH-SY5Y cells were reversely transfected with the 'Synthego Human Druggable Genome' sgRNA library and incubated for 72 hours. To ensure high consistency and minimize variability, we used automated systems, including sgRNA transfer, pipetting, and liquid dispensing. High-content imaging at 40× magnification was performed using the IXM high-content imaging system, followed by automated analysis of individual cells with hundreds of cells per well (*AP4B1*^{WT}:

930.342 ± 318.332, *AP4B1*^{KO}: 845.354 ± 289.564) using a custom pipeline developed with MetaXpress software. Cellular compartments were labeled with four markers: Hoechst 33258 (nucleus), β-Tubulin III (cytoskeleton), TGN46 (*trans*-Golgi network), and ATG9A (ATG9A compartment). To quantify ATG9A distribution, we calculated the ratio of ATG9A localized inside versus outside the TGN. Consistent with previous findings (9,10,26), *AP4B1*^{KO} cells showed distinct perinuclear accumulation of ATG9A overlapping with the TGN (*Fig. 1C, D*), resulting in a significantly elevated ATG9A ratio (*AP4B1*^{WT}: 1.276 ± 0.043, *AP4B1*^{KO}: 1.817 ± 0.213; $p < 0.001$, Cohen's $d \approx 2.74$).

The 'Synthego Human Druggable Genome' sgRNA library targets 8,478 genes, arrayed in a 384-well format, with designated spaces for assay-specific controls. To address potential off-target effects and transfection toxicity, we included negative controls such as *AP4B1*^{KO} cells transfected with sgRNAs targeting the non-essential genes *NLRP5* and *KRT77*, as well as untransfected *AP4B1*^{KO} cells. Positive controls included *AP4B1*^{WT} cells, either untransfected or transfected with sgRNAs targeting *NLRP5*. Additionally, *AP4B1*^{KO} cells transfected with sgRNAs targeting essential genes *COPA* and *KIF11* served as controls to assess transfection efficiency. sgRNAs targeting *ATG9A* in *AP4B1*^{KO} cells were used to evaluate the assay's sensitivity to dynamic changes in ATG9A trafficking (*Fig. S2A*).

Each library plate was screened in three technical replicates with high consistency across replicates demonstrated by Pearson's correlation coefficient (0.907 ± 0.035) (*Fig. 2A*). Quality metrics for high-throughput screening, including Z' and SSMD (robust versions

included), exceeded predefined thresholds (Z' and Z' robust > 0.3; SSMD and SSMD robust > 5) (*Fig. 2B*, *Fig. S2B–D*). Knockout of non-essential genes did not alter the ATG9A ratio in either *AP4B1*^{KO} or *AP4B1*^{WT} cells (*Fig. 2C*). However, minor reductions in cell count suggested low levels of toxicity from off-target effects (*Fig. 2D*). Knockout of *ATG9A* similarly reduced cell counts but significantly decreased the ATG9A ratio in *AP4B1*^{KO} cells, nearly matching levels observed in *AP4B1*^{WT} cells. This reduction was accompanied by diminished perinuclear ATG9A accumulation (*Fig. 2E*). As expected, knockout of essential genes induced apoptosis. For instance, sgRNAs targeting *COPA* reduced cell counts by approximately 52%, reflecting efficient transfection and knockout. Interestingly, *KIF11* knockout decreased cell counts by only 35%, possibly due to the reduced importance of *KIF11* in postmitotic SH-SY5Y cells (*Fig. 2D*).

Finally, analysis of the sgRNA library using Panther gene ontology (GO) terms revealed that most targeted genes encode metabolite interconversion enzymes, protein-modifying enzymes, transmembrane signal receptors and transporters (*Fig. 2F*).

Primary and Secondary Screens Identify Key Modulators of ATG9A Trafficking

As anticipated, the majority of the 8,478 genes screened did not significantly impact ATG9A distribution, as measured by the mean z-score robust of the ATG9A ratio across all three replicates (*Fig. 3A, B*). The z-score robust (not to be confused with Z') is a measure of the effect size calculated from the difference of a given value to the median in relation to the median absolute deviation. Since the screen aims for a reduction of the ATG9A ratio, the greatest negative z-scores are desired.

1,041 genes (12.28%) were found to decrease the cell count (z-score robust < -3 in two or more replicates) and were excluded from further analysis due to potential cytostatic or cytotoxic effects. Ultimately, 92 genes met the predefined threshold for ATG9A ratio reduction (z-score robust < -3 in all replicates), with a mean z-score robust across all replicates of -4.794 ± 1.123. This represents a hit rate of 1.09%, comparable to other high-throughput screening assays (29).

To refine our findings and eliminate false positives, we conducted a secondary screen on the 92 identified hits. An additional 58 genes were selected from the top of the list of genes meeting a slightly less stringent cutoff (ATG9A ratio: z-score robust < -3 in two replicates, z-score robust < -2 in all replicates, ranked by mean z-score robust of all replicates) (*Fig. S3A*). In re-screening these 150 top-listed genes, we followed the same experimental protocol as in the primary screen but extended the analysis to include a multi-parametric *trans*-Golgi network (TGN) morphology characterization, with the goal of identifying confounding effects on Golgi morphology that could impact the ATG9A ratio. Ultimately, 44 genes were confirmed to significantly impact ATG9A translocation: 14 genes consistently met the stringent z-score robust < -3 threshold across all replicates, while the remaining 30 genes satisfied a z-score robust < -2 in all replicates and < -3 in at least two replicates (*Fig. 4A*).

Most identified genes reduced the ATG9A ratio by decreasing ATG9A signal intensity inside the TGN, with minimal changes to ATG9A levels outside the TGN (*Fig. 4B*). Interestingly, three genes - *BTN2A1*, *EMILIN1*, and *MUC20* - primarily increased ATG9A

signal intensity outside the TGN (*Fig. 4C*). Additionally, several genes were found to enlarge the TGN area, potentially indicating either a reorganization of the TGN or early signs of cytotoxicity (*Fig. 4D*). The exact biological significance of this TGN enlargement remains unclear and warrants further investigation.

The data from primary and secondary screens are provided as supplementary files (*Supplementary Files 1 and 2*), offering a comprehensive resource for exploring the genetic modulators of ATG9A trafficking.

Pathway Analysis Illustrates Modulatory Landscape of ATG9A Trafficking

Hit identification in high-throughput screens based solely on ranked readout measures often overlooks the cumulative effects of functionally related genes that do not individually meet hit criteria. To address this limitation, we developed a customized pathway analysis specifically for arrayed high-throughput screens. Unlike conventional pathway analysis tools, our method incorporates the robust z-score for each gene rather than relying solely on its rank position. Inspired by an approach previously used in siRNA screens (30), we utilized a model that calculates the cumulative z-score robust adjusted for the pathway size (Pathway Impact (PI) Score) and determines the likelihood of obtaining a given PI score by chance (p-value). This model was applied to data from our primary screen. Ultimately, 463 out of 15,365 pathways (3.01%) were identified as significantly affected (*Fig. 5*, *Supplementary File 4*).

To better understand these pathways, we grouped functionally similar pathways into broader clusters by calculating genetic overlaps and constructing a similarity matrix. Following average linkage clustering, we applied the Dynamic Tree Cut algorithm – commonly used in gene expression analysis within the WGCNA package (31,32) – resulting in 12 distinct clusters (*Fig. 6A*). Each cluster was manually annotated with umbrella terms reflecting its primary function (*Table 1*). For each cluster, we calculated the mean PI Score and mean z-score (≙ mean p-value) (*Fig. 6B, C*). Cluster 4, encompassing GO terms related to potassium channel activity, exhibited the lowest mean z-score and the highest mean PI Score, indicating a substantial impact on ATG9A trafficking. Cluster 1, associated with oxidative degradation, also strongly influenced ATG9A distribution. Notably, cluster 6, comprising GO terms related to vesicular transport, demonstrated significant effects on ATG9A redistribution. Conversely, cluster 11 contained 99 pathways with no meaningful connections and was excluded from further analysis.

To characterize protein families driving these effects, we grouped proteins within the three most prominent clusters (lowest PI-score) based on their UniProt family annotations. Cluster 1 (oxidative degradation) predominantly featured proteins from the cytochrome P450 family. Cluster 4, consistently the most affected, was enriched with potassium channel family proteins, aligning with the GO terms associated with this cluster. Interestingly, cluster 6, linked to vesicular transport, primarily included members of the small GTPase superfamily, such as Rab and Arf family proteins, but also membrane fusion proteins including synaptobrevin and syntaxin family proteins (*Fig. 6D*). This

highlights the important role of small GTPases for ATG9A trafficking in AP-4 deficient cells, something that we have also identified in a previous small molecule screen (33).

Next, we integrated the pathway analysis findings with the results of the secondary screen. Approximately one third of the confirmed hits from the secondary screen were associated with significant pathways, spanning 8 clusters (*Fig. 7A*). Certain genes were exclusively linked to a single pathway cluster, such as *ARL5B* ('vesicular transport'), *ATF6B* ('cellular stress response'), *HEATR5B* ('vesicular transport'), *KCNQ4* ('potassium channel activity'), *NR3C1* ('histone H3 demethylation', *NUTF2* ('vesicular transport'), *TDP1* ('signal transduction') or *TNPO1* ('vesicular transport'). Others, such as *ADORA1* and *NPM1*, were connected to multiple clusters. Given the cellular phenotypes of AP4-deficiency syndrome, genes involved in vesicular transport (cluster 6) were of particular interest. Notably, *ARL5B*, *HEATR5B*, *NPM1, NUTF2* and *TNPO1* were associated with this cluster. Cluster 2 ('lipid metabolism') was represented by *ADORA1*.

To corroborate our findings, we compared the hits from the secondary screen with a recent study, which identified ATG9A interactors using quantitative BioID proteomics (34). Remarkably, three of our confirmed hits - *HEATR5B*, *MTMR14*, and *SNX29* - were also present in this dataset, highlighting their potential for follow-up studies. Additionally, we evaluated the availability of specific pharmacological inhibitors for the selected genes, facilitating potential clinical translation. We narrowed the list of secondary screen hits to those meeting at least one of the following criteria: (1) association with a relevant pathway cluster, (2) identification as an ATG9A interactor by BioID (34), and (3) availability of a

specific small molecule inhibitor (*Fig. 7B*). The top four hits - *ANPEP*, *NPM1*, *SNX29*, and *KCNQ4* - were prioritized for further validation experiments.

Validation Experiments Confirm *ANPEP* and *NPM1* as Potential Therapeutic Targets

To ensure the robustness of our findings from the primary and secondary screens, we performed validation experiments with multiple replicates based on nucleofection, a transfection method that achieves higher knockout efficiencies compared to lipofection used in the earlier screens. Knockout efficiency was confirmed via sequencing and analysis with the ICE tool provided by Synthego, which demonstrated knockout scores ranging from 80% to 100%. Moreover, diminished gene expression following knockout of target genes was separately confirmed on mRNA or protein level (*Fig. S5*).

Reevaluation of *ANPEP* (also known as *CD13*) and *NPM1* knockout confirmed their impact on the ATG9A ratio, consistent with the results from the primary and secondary screens. Conversely, knockout of *KCNQ4* and *SNX29* did not demonstrate a similar ATG9A translocation as seen in both screens (*Fig. 8A, B*). These findings further support the role of ANPEP and NPM1 in regulating ATG9A trafficking in AP4-deficient cells. A detailed analysis of various parameters of TGN integrity revealed less pronounced changes upon knockout of *ANPEP* compared to *NPM1* (*Fig. 8C*), suggesting that *ANPEP* plays a more specific role than *NPM1* in ATG9A trafficking without fundamentally disrupting TGN structure.

To assess the broader effects of *ANPEP* and *NPM1* knockouts on cell morphology, we conducted multiparametric profiling using 25 parameters characterizing the cytoskeleton (i.e. cell shape), nucleus and TGN. Dimensionality reduction by principal component analysis (PCA) across these cellular morphology metrics revealed substantial differences between the two knockouts. *ANPEP* knockout exhibited considerably less variability in cellular morphology compared to *NPM1* knockout, underscoring the lower toxicity associated with *ANPEP* disruption (*Fig. 8D*). This finding highlights *ANPEP* as a promising target for further therapeutic exploration, with a more favorable toxicity profile than *NPM1*.

DISCUSSION

Despite considerable progress in recent years, the molecular mechanisms underlying AP-4-associated HSP remain incompletely understood. Deciphering these cellular processes is critical for developing new therapeutic strategies for this progressive childhood-onset disease. In this study, we conducted a phenotypic high-content arrayed CRISPR/Cas9-based loss-of-function screen in a neuronal model of AP-4 deficiency, revealing key pathways and identifying modulators of ATG9A trafficking in the context of AP-4 deficiency.

CRISPR/Cas-based functional genomics screens have proven to be a powerful tool for elucidating gene and pathway function. Leveraging the advantages of CRISPR technology over previous genomic screening methods, we interrogated a library targeting approximately one-third of the human genome. To achieve this, we developed an arrayed

screening platform using a neuronal cell model of AP-4 deficiency syndrome. By combining this platform with imaging-based multiparametric single-cell analysis, we demonstrated the strengths of arrayed CRISPR screening - offering high accuracy in gene function interrogation alongside a custom experimental and analytical pipeline. A robust assay design, including multiple replicates, stringent controls, and extensive automation, allowed us to maximize the utility of this approach (35).

We acknowledge several limitations of this study. First, SH-SY5Y cells represent a well-established and widely used model for neuronal biology and neurodegenerative disease research. Upon differentiation, they exhibit acquire key neuronal features, including expression of neuronal markers and neurite formation (28), while remaining experimentally tractable for large-scale perturbation approaches such as high-content CRISPR screening. These properties make them particularly suitable for discovery-oriented screening campaigns requiring scalability, reproducibility, and robust phenotypic readouts. However, as a neuroblastoma-derived cell line, SH-SY5Y cells do not fully recapitulate the molecular and functional characteristics of mature postmitotic neurons. More physiologically relevant systems, including induced pluripotent stem cell (iPSC)-derived neurons, may provide complementary platforms to validate and further investigate candidate regulators identified in this screen, although these systems are less amenable to high-throughput approaches.

Second, the alphabetical arrangement of the sgRNA library in the primary screen introduced the potential for plate-based artifacts. To mitigate this risk, we applied stringent

quality control criteria and performed a secondary screen with randomized plate layouts, which substantially reduced the likelihood of systematic bias. Third, the transfection efficiency achieved using lipofection may have limited sensitivity, potentially resulting in false negatives for genes with more subtle phenotypic effects. Despite these limitations, our approach identified multiple candidate regulators of ATG9A distribution in AP-4-deficient cells.

Notably, several of the identified genes have established roles in neurological disease. These include *ADAM22*, where biallelic variants are associated with progressive encephalopathy and infantile-onset refractory epilepsy (36); *NR2F1*, where haploinsufficiency is linked to Bosch-Boonstra-Schaaf optic atrophy syndrome (37); biallelic variants in *NTRK1*, implicated in hereditary sensory and autonomic neuropathy type IV (HSAN IV) (38); and *TDP1*, associated with spinocerebellar ataxia with axonal neuropathy (SCAN1) (39). Other hits are linked to non-neurological disorders but converge on pathways of potential relevance to neuronal homeostasis. For example, *MTMR14*, which is implicated in centronuclear myopathy (40,41), functions as a negative regulator of autophagy initiation (42). Pharmacological inhibition of MTMR14 has been shown to enhance autophagic flux and mitigate disease progression in models of neurodegeneration (43).

Consistent with the central role of AP-4 in vesicular trafficking and autophagy, several identified genes are directly connected to autophagic pathways. TMEM59, an endosomal transmembrane protein, promotes selective autophagy by facilitating LC3 recruitment and

subsequent lysosomal degradation of endosomal compartments (44). Loss of TMEM59 has been reported to ameliorate disease-relevant phenotypes in a tauopathy mouse model (45). In addition, broader regulators of cellular homeostasis were identified, including ATF6B, a key sensor of endoplasmic reticulum stress within the unfolded protein response (46). Emerging evidence further supports a role for ATF6B in embryonic brain development (47).

Our pathway analysis highlighted several clusters and protein classes as critical modulators of AP-4 deficiency syndrome, offering potential therapeutic targets. As anticipated, proteins involved in vesicular transport emerged as key regulators. Specifically, we identified small GTPases from the Rab and Arf families as essential regulators.

This aligns with previous studies implicating small GTPases in ATG9A and AP-4 cycling. For example, Rab7 has been shown to regulate the recruitment of ATG9A-positive vesicles for mitophagy (48), while Rab1 is essential for autophagosome formation and is present on ATG9A vesicles (49). Beyond this, Rab10 is necessary for ATG-9 trafficking in *Caenorhabditis elegans* (50). Our group previously demonstrated that small molecules targeting Rab3C and Rab12 can restore ATG9A distribution in AP-4-deficient cells (33). Arf-like proteins also play crucial roles; for instance, Arl5b, regulates retrograde endosome-to-TGN transport (51,52). In our screen, loss of Arl5b significantly promoted ATG9A redistribution. Potentially, this is mediated by diminished retrograde transport of ATG9A to the TGN.

Another hit, *NR3C1*, encodes for a nuclear glucocorticoid receptor and is related to the significant pathway cluster 'histone H3 demethylation'. In mouse pancreatic β cells, NR3C1 was found to enhance autophagy via increased expression of the RNA demethylase FTO (fat mass and obesity-associated protein). FTO catalyzes m^6A demethylation of *Atg9a* which promotes mRNA stability and thereby upregulates *Atg9a* expression (53). Consequently, knockout of *NR3C1* in our screen likely lowered *ATG9A* expression and reduced its accumulation in the TGN.

The conservation of AP-4-mediated vesicular transport across eukaryotes is striking; plants exhibit similar cellular phenotypes to mammalian cells in the context of AP-4 deficiency (54,55). In *Arabidopsis thaliana* seedlings, AP-4 loss depleted cytochrome P450 proteins (55). In our pathway analysis, cluster 1 dominated by cytochrome P450 enzymes was among the top three clusters, suggesting a conserved role for these enzymes in AP-4-dependent vesicular trafficking. Additionally, lipid metabolism pathways (cluster 2) emerged as relevant. The diverse interconnections between AP-4 and lipid metabolism have been established in both human cells and mouse models, i.e. by the identification of AP-4 cargos such as low-density lipoprotein receptor (LDLR) and diacylglycerol lipase beta (DAGLB) (16,56). Furthermore, altered trafficking of the AP-4 cargo ApoER2 (apolipoprotein E receptor 2) in AP-4 deficient cells implicated aberrant Reelin signaling (57).

Interestingly, our screen uncovered cation channels, particularly potassium channels, as modulators of ATG9A cycling. Two hits from the secondary screen, *KCNQ4* and *TPCN2*, are prominent representatives. TPC2, a non-selective cation channel localized to endolysosomal membranes encoded by the *TPCN2* gene, is involved in intracellular transport and lysosomal exocytosis, and has been investigated as a therapeutic target for lysosomal storage diseases and neurodegenerative disorders (58). However, KCNQ4, a potassium channel critical for neuronal excitability in cochlear sensory cells (59), together with SNX29, a cellular trafficking protein with a phospholipid-binding domain (60) that has been suggested to be associated with mental disorders (61), showed inconsistent results upon repeated testing. This highlights the challenges of validating subtle phenotypic changes in high-content screens.

Among the confirmed hits, *ANPEP* and *NPM1* emerged as strong candidates for further exploration. Knockout of both genes consistently influenced ATG9A redistribution. However, the impact of *ANPEP* knockout on TGN morphology was less pronounced. This suggested a more specific modulation of ATG9A trafficking, whereas *NPM1* knockout implicated a less targeted effect which resulted in TGN disruption, possibly causing unselective cargo escape. ANPEP, also referred to as CD13, is a membrane-associated protein with aminopeptidase activity. Beyond its enzymatic function, ANPEP exhibits pleiotropic roles and has been described as a 'moonlighting protein' (62). It mediates multiple non-enzymatic processes, including regulation of endosomal trafficking and modulation of intracellular signaling pathways such as MAPK, PI3K, and NF-κB (63). In addition, ANPEP has been linked to autophagy through the upregulation of ATG7

expression in human hepatoma cells (64). Its potential involvement in TGN protein export, however, represents a previously unrecognized function. Given its robust effect on ATG9A trafficking and the limited toxicity observed in our system, ANPEP emerges as a candidate for further therapeutic investigation.

In summary, our study provides insights into the mechanisms regulating ATG9A trafficking in AP4-deficient neuronal cells. We identified candidate genes, such as *ANPEP*, that warrant further investigation as potential drug targets for AP4-HSP. Additionally, we present a comprehensive dataset for the research community and outline an experimental and analytical pipeline that serves as a blueprint for future arrayed cell-based phenotypic screens.

METHODS

Sex as a biological variable

This study used SH-SY5Y cells, a cell line originally derived from a female patient. Sex itself was not considered a biological variable; we assume that the results of our study are similarly applicable to all sexes.

Key resources table

Please refer to Supplementary Table 1.

Experimental model and study participant details

SH-SY5Y Cells

For this study, we used previously published SH-SY5Y cells stably expressing a sgRNA targeting *AP4B1* and Cas9, and SH-SY5Y cells stably expressing Cas9 but no sgRNA.(10) Cells were cultured in Dulbecco's Modified Eagle Medium/Nutrient Mixture F-12 supplemented with 10% Fetal Bovine Serum (FBS), 100 U/mL penicillin, and 100 µg/mL streptomycin. Cultures were maintained at 37°C in a humidified incubator with 5% CO_2. Cells were passaged every three days by washing with Dulbecco's phosphate-buffered saline (DPBS) and dissociating with 0.25% Trypsin-EDTA. Media changes were performed every other day to ensure optimal growth conditions. For differentiation, SH-SY5Y cells were cultured in neurobasal medium supplemented with 1× B-27 supplement, 2 mM L-glutamine, and 10 µM all-*trans* retinoic acid for five days. To improve differentiation and enhance cell attachment, laminin (10 µg/mL) was added to the differentiation media.(65)

SgRNA Library

The ‘Synthego sgRNA Human Druggable Genome’ library was obtained from the ICCB Longwood Screening Facility at Harvard Medical School. This library targets 8,478 human genes, utilizing three distinct chemically synthesized sgRNAs per gene, each designed to target early exons. The library is arrayed across 29 plates in a 384-well format, with designated wells allocated for assay-specific controls to ensure experimental consistency.

Method details

Reverse Transfection

All steps were conducted in an RNase- and DNase-free environment to ensure sample integrity. Positive and negative control sgRNAs (targeting *ATG9A* and *NLRP5*, respectively) were diluted in nuclease-free Tris-EDTA buffer and dispensed into the appropriate wells of a 384-well PCR plate to achieve a final concentration of 50 nM. Lipofectamine™ RNAiMAX transfection reagent was diluted in reduced-serum medium (Opti-MEM) and distributed into three 384-well assay plates per library plate to create three replicates. The final volume of RNAiMAX in the reaction was adjusted to 0.16%. The sgRNA library and control sgRNAs were transferred to the RNAiMAX-containing assay plates using the Agilent Bravo Automated Pipettor and the Agilent 4-R BenchCel Plate Handler. SH-SY5Y cells cultured in differentiation media for two days were counted using an automated cell counter. Cells were then plated at a density of 3,000 cells per well in differentiation media containing 10 μM all-*trans* retinoic acid, but without laminin.

The Multidrop™ Combi Reagent Dispenser was employed for RNAiMAX solution dispensing and cell plating. Plates were spun briefly to ensure even distribution of reagents and incubated at room temperature for 20 minutes to allow uniform cell settlement. The assay plates were incubated for 72 hours at 37°C in a 5% CO_2 humidity-controlled incubator to minimize evaporation and edge effects. After 24 hours of incubation, 10% differentiation media supplemented with 40 µM all-*trans* retinoic acid and 10 µg/mL laminin was added to support differentiation and cell adhesion.

Nucleofection

All steps were conducted in an RNase- and DNase-free environment to maintain sample integrity. To enhance gene-editing efficiency, ribonucleoprotein complexes (RNPs) were utilized for nucleofection. sgRNAs were diluted in TE buffer to a stock concentration of 100 µM, and Cas9 was prepared at a stock concentration of 20 µM. The nucleofector solution was prepared by mixing the nucleofector reagent and supplement at a 4.5:1 ratio. RNPs were assembled by combining sgRNA (final concentration: 7.2 µM) and Cas9 protein (final concentration: 0.8 µM) in the nucleofector solution. Briefly, 180 pmol sgRNA was incubated with 20 pmol Cas9 protein in the nucleofector solution for at least 10 minutes to form RNP complexes. SH-SY5Y cells were harvested, and 4×10^5 cells were resuspended in 5 µL of the prepared nucleofector solution. The cell suspension was mixed with the pre-assembled RNPs at a 1:6 ratio (cell suspension/RNP solution) and transferred into nucleofection strips. The strips were placed in the 4D-Nucleofector System, and nucleofection was carried out using the CA-137 program. After nucleofection, pre-warmed medium was added to the cells following a 10-minute

incubation at room temperature. The cells were subsequently plated at a density of 1 × 10^4 cells per well into a 96-well plate using the Integra Voyager 8-channel automated pipettor.

Fixation and Immunocytochemistry

After 72 hours of incubation, cells were fixed with 4% paraformaldehyde for 20 minutes at room temperature. Cells were then permeabilized using 0.1% saponin in DPBS for 10 minutes. Following permeabilization, the solution was removed and blocking buffer containing 0.1% bovine serum albumin (BSA) and 0.01% saponin in DPBS was added for 20 minutes to minimize non-specific binding. Primary antibodies were diluted in blocking buffer to the following concentrations: rabbit anti-ATG9A (1:500 to 1:1000), sheep anti-TGN46 (1:800), and mouse anti-β-Tubulin III (1:1000). Cells were incubated with primary antibodies for 1 hour at room temperature and then washed three times with blocking buffer. Secondary antibodies were prepared in blocking buffer at concentrations of 1:1250 to 1:2000 and included Alexa Fluor 488-conjugated anti-rabbit, Alexa Fluor 594-conjugated anti-sheep, and Alexa Fluor 647-conjugated anti-mouse. Additionally, Hoechst 33258 (1:2000) was used for nuclear staining. Cells were incubated with secondary antibodies for 30 minutes in the dark, followed by three washes with DPBS to remove unbound antibodies. All solutions used for immunostaining were filtered through a 0.22 μM filter system to ensure sterility and consistency. After staining, plates were sealed with opaque seals to prevent light exposure and prepared for imaging.

High-Throughput Imaging

High-throughput imaging in 384-well plates was performed using the Molecular Devices ImageXpress Micro Confocal Laser System, equipped with a 40× S Plan Fluor objective (numerical aperture: 0.60 µm, working distance: 3.6–2.8 mm). For each well, 16 fields were acquired in a 4 × 4 grid configuration. For high-throughput imaging in 96-well plates, 24 sites per well were captured in a 5 × 5 grid configuration, leaving out the center position. Sites were spaced 330 µm apart to ensure even coverage of each well. A PAA GX™ robot arm was used for automated plate loading into the microscope. Image analysis was conducted using a customized pipeline within the MetaXpress software (Molecular Devices, version 6.7.1.157). Cells were identified as β-Tubulin III-positive areas containing Hoechst-positive nuclei. The *trans*-Golgi network (TGN) was defined by TGN46 signal intensity, while ATG9A protein was identified based on its specific signal intensity. Overlapping TGN46 and ATG9A signals were classified as 'ATG9A inside the TGN', whereas ATG9A signal outside the TGN46-defined region but within the cellular boundary was categorized as 'ATG9A outside the TGN'.

Western Blotting

Cells were cultured in 6-well plates at a density of 5 × 10^5 cells per well and harvested using RIPA buffer supplemented with protease inhibitors and phosphatase inhibitors. The total protein concentration was determined using the Pierce™ BCA Protein Assay Kit with absorbance measured at 562 nm using a Tecan plate reader. Protein samples were adjusted to a total amount of 15 µg, mixed with NuPAGE™ LDS Sample Buffer, and supplemented with NuPAGE™ Sample Reducing Agent. The samples were boiled at 70°C for 10 minutes before loading onto NuPAGE™ 4–12% Bis-Tris gels. Electrophoresis

was carried out in NuPAGE™ MOPS SDS Running Buffer for approximately 50 minutes at 200 V. Proteins were transferred onto an Immobilon®-FL PVDF Membrane using a wet transfer system with NuPAGE™ Transfer Buffer at 30 V for 75 minutes. The membrane was then blocked with Intercept® (TBS) Blocking Buffer for 60 minutes on a shaker. Membranes were incubated overnight at 4°C with the following primary antibodies, diluted in Intercept® (TBS) Blocking Buffer supplemented with 0.2% TWEEN® 20:

- Mouse anti-CRISPR-Cas9 (1:500) (two-day incubation),
- Rabbit anti-AP4B1 (1:500),
- Mouse anti-β-Actin (1:2000),
- Mouse anti-AP4E1 (1:500),
- Rabbit anti-ATG9A (1:500).

Near-infrared secondary antibodies (IRDye® 800CW Donkey anti-Rabbit IgG; IRDye® 680LT Donkey anti-Mouse IgG) were diluted 1:5000 in Intercept® (TBS) Blocking Buffer supplemented with 0.2% TWEEN® 20 and 0.01% sodium dodecyl sulfate. Membranes were incubated with secondary antibodies for 1 hour at room temperature in the dark. Protein detection and imaging were performed using the LI-COR Odyssey® DLx system. Image analysis was carried out using the Image Studio software (LI-COR, version 5.2.5).

RT-QPCR

Total RNA was extracted using the RNeasy Mini Kit (QIAGEN, #74106). cDNA was synthesized using the High-Capacity cDNA Reverse Transcription Kit (Thermo Fisher Scientific, #4368813), following the manufacturer's protocol. Quantitative PCR was

performed using SYBR Green PCR Master Mix (Thermo Fisher Scientific, #4334973). Amplification was carried out on a QuantStudio 6 Flex Real-Time PCR System (Applied Biosystems) under standard cycling conditions. Melt curve analysis was included to verify product specificity.

Ct values were normalized to the mean of the housekeeping gene *RPL32*. Primer sequences are provided in the key resource table.

Available Small Molecule Inhibitors

Available small molecule inhibitors for prioritizing secondary screen hits (*Fig. 4B*) were identified using the 'International Union of Basic and Clinical Pharmacology (IUPHAR) / British Pharmacological Society (BPS) Guide to Pharmacology' (https://www.guidetopharmacology.org, accessed: 02/18/2025) and the product portfolio of MedChemExpress® (https://www.medchemexpress.com, accessed: 02/18/2025).

Quantification and statistical analysis

Statistical analysis and plotting were performed using R statistical computing (version 4.2.0) and the RStudio IDE (version 2022.12.0+353). The following R packages were used: dplyr (66), ggplot2 (67), openxlsx (68), ggpubr (69), plotly (70), ggrepel (71), ggExtra (72), janitor (73), lsr (74), tidyr (75), tibble (76), ComplexHeatmap (77,78), multcomp (79), effectsize (80), bibtex (81), UniprotR (82), dynamicTreeCut (83), ggbreak (84), gggap (85), pbapply (86), cluster (87), purr (88), moduleColor (89), pals (90), Hmisc (91), biomaRt (92,93), scales (94), RColorBrewer (95), circlize (96).

For normalization, the z-score robust was calculated:

$$z\,(robust)\,(x) = \frac{x - Median}{1.4826 * \ MAD}$$

(x: value per well, Median: median of all wells, MAD: median absolute deviation, 1.4826: constant to adjust MAD for asymptomatically normal consistency)

As a quality metric for assay plates to account for plating artefacts and staining irregularities, we calculated the Z' factor and the SSMD as well as the robust version of both parameters using the median and median absolute deviation.

$$Z' = 1 - \frac{3 * (SD\,(positive\ controls) + SD\,(negative\ controls))}{|mean\,(positive\ controls) - mean\,(negative\ controls)|}$$

$$Z'\,(robust) = 1 - \frac{3 * (MAD\,(positive\ controls) + MAD\,(negative\ controls))}{|Median\,(positive\ controls) - Median\,(negative\ controls)|}$$

$$SSMD = \frac{Mean\,(negative\ controls) - Mean\,(positive\ controls)}{\sqrt{(SD\,(negative\ controls))^2 + \ (SD\,(positive\ controls))^2}}$$

$$SSMD\,(robust) = \frac{Median\,(negative\ controls) - Median\,(positive\ controls)}{\sqrt{(MAD\,(negative\ controls))^2 + \ (MAD\,(positive\ controls))^2}}$$

Data is summarized by mean ± standard deviation. The Pearson correlation coefficient was calculated between all replicates using the *cor()* function in R. Statistical differences

between two groups were evaluated using two-sided Student's t-test, with p-values < 0.05 considered statistically significant. Effect sizes for two-group comparisons were estimated using Cohen's d, with the following thresholds applied: a Cohen's d of ≤ 0.2 indicated a small effect, 0.5 a medium effect, and ≥ 0.8 a large effect (97). For comparisons involving multiple groups, one-way analysis of variance (ANOVA) was used, followed by Tukey's HSD or Dunnett's multiple comparison post-hoc test for comparisons to the control group. Effect sizes for multiple group comparisons were estimated using eta squared (η^2), with thresholds defined as: $\eta^2 \leq 0.01$ indicating a small effect, $\eta^2 = 0.06$ a medium effect, and $\eta^2 \geq 0.14$ a large effect (97). A total of three wells in the *AP4B1*^{KO} + *NLRP5* control group were excluded from analysis due to screening artifacts.

The morphological profile of the TGN was analyzed using TGN roughness (shape factor in the MetaXpress software) and the following calculated metrics:

$$TGN\ Elongation = \frac{TGN\ With}{TGN\ Length}$$

$$TGN\ Compactness = \frac{(TGN\ Perimeter)^2}{4\pi * TGN\ Area}$$

For pathway analysis, a list of GO terms associated with genes from the screen was derived from Ensembl (*Supplementary File 3*). GO terms with less than 3 or more than 1,000 genes in our screen were excluded. For each GO term, a Pathway Impact Score (PI Score) was calculated (30).

$$PI = \frac{\sum_{i=1}^{n} z\ robust\ i}{\sqrt{n}}$$

(PI: Pathway Impact Score, n = number of genes associated with GO term, z robust i: z-score robust for each gene associated with GO term)

The Pathway Impact Score calculation for each GO term size, i.e. the number of genes comprised by each GO term, was performed 10,000 times using randomly selected values from the screen for the z-score robust. From this, the normal distribution of PI scores for each GO term could be derived and the probability p of obtaining the actual PI score by chance was calculated. Similar sized GO terms yielded a similar normal distribution. Therefore, p-values were adjusted for multiple testing according to Bonferroni by multiplication with the number of occurrences of the respective GO term size. A pathway was considered significantly affected if p adjusted < 0.05.

To determine the overlap between two pathways, we calculated the overlap coefficient (30).

$$O(i,j) = \frac{|Si \cap Sj|}{\min(|Si|, |Sj|)}$$

$|Si \cap Sj|$ is the number of shared genes between the two gene sets Si and Sj, $\min(|Si|, |Sj|)$ is the size of the smaller set.

A matrix of overlap coefficients was calculated for all pathways. From this, a distance matrix based on Euclidean distance was generated, followed by average linkage clustering. The hierarchical clustering order was applied to reorder the overlap coefficient matrix, and a heatmap view was created for visualization. Clusters of highly overlapping pathways were identified using the 'Dynamic Tree Cut' algorithm (83). Suitable umbrella terms were manually assigned to each cluster to provide descriptive labels. For the proteins associated with each cluster, family domain information was retrieved from the Universal Protein Resource (UniProt) (82).

Plotting and statistical analysis for *Fig. S5* was performed using GraphPad Prism version 10, GraphPad Software.

Additional resources

The Synthego sgRNA Human Druggable Genome Library is available through the ICCB-Longwood Screening Facility at Harvard Medical School:
https://iccb.med.harvard.edu/synthego-sgrna-human-druggable-genome

Detailed nucleofection protocol for Lonza 4D Nucleofector:
https://bioscience.lonza.com/lonza_bs/DE/en/document/21324

Study approval

No human or animal studies were conducted.

Data availability

- Screening data have been deposited at Zenodo and are publicly available as of the date of publication. *DOI:* 10.5281/zenodo.10574989
- Relevant original code has been deposited at Zenodo and is publicly available as of the date of publication. *DOI:* 10.5281/zenodo.10574989
- Any additional information required to reanalyze the data reported in this paper is available from the lead contact upon request.
- Source data for figures is available in the supporting data values file

Further information and requests for resources and reagents should be directed to and will be fulfilled by the lead contact, Darius Ebrahimi-Fakhari, MD, PhD (darius.ebrahimi-fakhari@childrens.harvard.edu).

AUTHOR CONTRIBUTIONS

M.Z., C.G., J.E.A, X.X., A.S., A.K.D., D.E.F. conceptualized and designed the experiments. M.Z., C.G., J.E.A, X.X., H.M.K., D.E.F. performed experiments. M.Z. and D.E.F. wrote the first draft of the manuscript. All authors contributed to the final draft of the manuscript. D.E.F. wrote the grants that designed and supported this project. D.E.F. supervised the project. C.G. and J.E.A. contributed equally to this work. C.G. is listed first in recognition of contributions made at later stages of the project.

FUNDING SUPPORT

This work is the result of NIH funding, in whole or in part, and is subject to the NIH Public Access Policy. Through acceptance of this federal funding, the NIH has been given a right to make the work publicly available in PubMed Central.

- CureAP4 Foundation (to D.E.-F.)
- Spastic Paraplegia Foundation (to D.E.-F.)
- Manton Center for Orphan Disease Research (to D.E.-F.)
- BCH Office of Faculty Development (to D.E.-F.)
- BCH Translational Research Program (to D.E.-F.)
- National Institute of Neurological Disorders and Stroke grant no. 1K08NS123552-01 and 1U54NS148312 (to D.E.-F.)
- German National Academic Foundation (to M.Z., C.G., J.E.A)
- Bayer Foundation, Carl Duisberg Fellowship for Medical Sciences (to M.Z.)
- German National Exchange Service, Biomedical Education Program (to M.Z., C.G., J.E.A)
- RWTH-Aachen-Research-Ambassador-Scholarship (to C.G.)
- German Research Foundation, grant no. 448402208 (to A.S.)
- European Union's Horizon 2020 research and innovation program, the Marie Sklodowska-Curie grant agreement no. 896725 (to A.K.D)
- Rosamund Stone Zander chair (to M.S.)
- National Institutes of Health, grant 1U54HD090255 (to IDDRC at Boston Children's Hospital)

ACKNOWLEDGEMENTS

The authors thank Jennifer Smith, PhD, Clarence Yapp, PhD, and the team at the ICCB-Longwood Screening Facility for their assistance in designing and conducting the screening experiments. We also gratefully acknowledge Dr. Bechara Kachar (National Institute on Deafness and Other Communication Disorders, NIDCD) for the generous gift of the anti-KCNQ4 antibody.

REFERENCES

1. Wallin E, von Heijne G. Genome-wide analysis of integral membrane proteins from eubacterial, archaean, and eukaryotic organisms. Protein Sci. 1998 Apr;7(4):1029–38. doi:10.1002/pro.5560070420 PubMed PMID: 9568909.
2. Stevens TJ, Arkin IT. Do more complex organisms have a greater proportion of membrane proteins in their genomes? Proteins. 2000 Jun;39(4):417–20. doi:10.1002/(sici)1097-0134(20000601)39:4<417::aid-prot140>3.0.co;2-y PubMed PMID: 10813823.
3. Tan JZA, Gleeson PA. The role of membrane trafficking in the processing of amyloid precursor protein and production of amyloid peptides in Alzheimer's disease. Biochim Biophys Acta Biomembr. 2019 Apr;1861(4):697–712. doi:10.1016/j.bbamem.2018.11.013 PubMed PMID: 30639513.
4. De Matteis MA, Luini A. Mendelian disorders of membrane trafficking. N Engl J Med. 2011 Sep;365(10):927–38. doi:10.1056/NEJMra0910494 PubMed PMID: 21899453.
5. Ebrahimi-Fakhari D, Behne R, Davies AK, Hirst J. AP-4-Associated Hereditary Spastic Paraplegia. In: Adam MP, Ardinger HH, Pagon RA, Wallace SE, Bean LJH, Mirzaa G, et al., editors. GeneReviews(®). Seattle (WA): University of Washington, Seattle Copyright © 1993-2021, University of Washington, Seattle. GeneReviews is a registered trademark of the University of Washington, Seattle. All rights reserved.; 2018. PubMed PMID: 30543385.
6. Ebrahimi-Fakhari D, Teinert J, Behne R, Wimmer M, D'Amore A, Eberhardt K, et al. Defining the clinical, molecular and imaging spectrum of adaptor protein complex 4-associated hereditary spastic paraplegia. Brain. 2020/09/27. 2020;143(10):2929–44. doi:10.1093/brain/awz307 PubMed PMID: 32979048.
7. Ebrahimi-Fakhari D, Alecu JE, Ziegler M, Geisel G, Jordan C, D'Amore A, et al. Systematic Analysis of Brain MRI Findings in Adaptor Protein Complex 4-Associated Hereditary Spastic Paraplegia. Neurology. 2021 Nov;97(19):e1942–54. doi:10.1212/WNL.0000000000012836 PubMed PMID: 34544818.
8. Ebrahimi-Fakhari D, Cheng C, Dies K, Diplock A, Pier DB, Ryan CS, et al. Clinical and genetic characterization of AP4B1-associated SPG47. Am J Med Genet A. 2017/12/02. 2018;176(2):311–8. doi:10.1002/ajmg.a.38561 PubMed PMID: 29193663.
9. Mattera R, Park SY, De Pace R, Guardia CM, Bonifacino JS. AP-4 mediates export of ATG9A from the trans-Golgi network to promote autophagosome formation. Proc Natl Acad Sci U S A. 2017/11/29. 2017;114(50):E10697-e10706. doi:10.1073/pnas.1717327114 PubMed PMID: 29180427.
10. Davies AK, Itzhak DN, Edgar JR, Archuleta TL, Hirst J, Jackson LP, et al. AP-4 vesicles contribute to spatial control of autophagy via RUSC-dependent peripheral delivery of ATG9A. Nat Commun. 2018/09/29. 2018;9(1):3958. doi:10.1038/s41467-018-06172-7 PubMed PMID: 30262884.
11. Ivankovic D, Drew J, Lesept F, White IJ, López Doménech G, Tooze SA, et al. Axonal autophagosome maturation defect through failure of ATG9A sorting underpins pathology in AP-4 deficiency syndrome. Autophagy. 2019/05/31. 2020;16(3):391–407. doi:10.1080/15548627.2019.1615302 PubMed PMID: 31142229.

12. Behne R, Teinert J, Wimmer M, D'Amore A, Davies AK, Scarrott JM, et al. Adaptor protein complex 4 deficiency: a paradigm of childhood-onset hereditary spastic paraplegia caused by defective protein trafficking. Hum Mol Genet. 2020/01/10. 2020;29(2):320–34. doi:10.1093/hmg/ddz310 PubMed PMID: 31915823.
13. D'Amore A, Tessa A, Naef V, Bassi MT, Citterio A, Romaniello R, et al. Loss of ap4s1 in zebrafish leads to neurodevelopmental defects resembling spastic paraplegia 52. Ann Clin Transl Neurol. 2020/03/28. 2020;7(4):584–9. doi:10.1002/acn3.51018 PubMed PMID: 32216065.
14. De Pace R, Skirzewski M, Damme M, Mattera R, Mercurio J, Foster AM, et al. Altered distribution of ATG9A and accumulation of axonal aggregates in neurons from a mouse model of AP-4 deficiency syndrome. PLoS Genet. 2018/04/27. 2018;14(4):e1007363. doi:10.1371/journal.pgen.1007363 PubMed PMID: 29698489.
15. Mattera R, Williamson CD, Ren X, Bonifacino JS. The FTS-Hook-FHIP (FHF) complex interacts with AP-4 to mediate perinuclear distribution of AP-4 and its cargo ATG9A. Mol Biol Cell. 2020/02/20. 2020;31(9):963–79. doi:10.1091/mbc.E19-11-0658 PubMed PMID: 32073997.
16. Matsuda S, Miura E, Matsuda K, Kakegawa W, Kohda K, Watanabe M, et al. Accumulation of AMPA Receptors in Autophagosomes in Neuronal Axons Lacking Adaptor Protein AP-4. Neuron. 2008;57(5):730–45. doi:https://doi.org/10.1016/j.neuron.2008.02.012
17. Buehler E, Chen YC, Martin S. C911: A bench-level control for sequence specific siRNA off-target effects. PLoS One. 2012;7(12):e51942. doi:10.1371/journal.pone.0051942 PubMed PMID: 23251657.
18. Krueger U, Bergauer T, Kaufmann B, Wolter I, Pilk S, Heider-Fabian M, et al. Insights into effective RNAi gained from large-scale siRNA validation screening. Oligonucleotides. 2007;17(2):237–50. doi:10.1089/oli.2006.0065 PubMed PMID: 17638527.
19. Agrotis A, Ketteler R. A new age in functional genomics using CRISPR/Cas9 in arrayed library screening. Front Genet. 2015;6:300. doi:10.3389/fgene.2015.00300 PubMed PMID: 26442115.
20. Emanuel G, Moffitt JR, Zhuang X. High-throughput, image-based screening of pooled genetic-variant libraries. Nat Methods. 2017 Dec;14(12):1159–62. doi:10.1038/nmeth.4495 PubMed PMID: 29083401.
21. Lawson MJ, Camsund D, Larsson J, Baltekin Ö, Fange D, Elf J. In situ genotyping of a pooled strain library after characterizing complex phenotypes. Mol Syst Biol. 2017 Oct;13(10):947. doi:10.15252/msb.20177951 PubMed PMID: 29042431.
22. Guerriero ML, Corrigan A, Bornot A, Firth M, O'Shea P, Ross-Thriepland D, et al. Delivering Robust Candidates to the Drug Pipeline through Computational Analysis of Arrayed CRISPR Screens. SLAS Discov. 2020 Jul;25(6):646–54. doi:10.1177/2472555220921132 PubMed PMID: 32394775.
23. Kim HS, Lee K, Kim SJ, Cho S, Shin HJ, Kim C, et al. Arrayed CRISPR screen with image-based assay reliably uncovers host genes required for coxsackievirus infection. Genome Res. 2018 Jun;28(6):859–68. doi:10.1101/gr.230250.117 PubMed PMID: 29712754.
24. O'Shea P, Wildenhain J, Leveridge M, Revankar C, Yang JP, Bradley J, et al. A Novel Screening Approach for the Dissection of Cellular Regulatory Networks of NF-κB Using

Arrayed CRISPR gRNA Libraries. SLAS Discov. 2020 Jul;25(6):618–33. doi:10.1177/2472555220926160 PubMed PMID: 32476557.
25. de Groot R, Lüthi J, Lindsay H, Holtackers R, Pelkmans L. Large-scale image-based profiling of single-cell phenotypes in arrayed CRISPR-Cas9 gene perturbation screens. Mol Syst Biol. 2018 Jan;14(1):e8064. doi:10.15252/msb.20178064 PubMed PMID: 29363560.
26. Ebrahimi-Fakhari D, Alecu JE, Brechmann B, Ziegler M, Eberhardt K, Jumo H, et al. High-throughput imaging of ATG9A distribution as a diagnostic functional assay for adaptor protein complex 4-associated hereditary spastic paraplegia. Brain Commun. 2021;3(4):fcab221. doi:10.1093/braincomms/fcab221 PubMed PMID: 34729478.
27. Ziegler M, Russell BE, Eberhardt K, Geisel G, D'Amore A, Sahin M, et al. Blended Phenotype of Silver-Russell Syndrome and SPG50 Caused by Maternal Isodisomy of Chromosome 7. Neurol Genet. 2021/02/09. 2021;7(1):e544. doi:10.1212/nxg.0000000000000544 PubMed PMID: 33553621.
28. Kovalevich J, Langford D. Considerations for the use of SH-SY5Y neuroblastoma cells in neurobiology. Methods Mol Biol. 2013;1078:9–21. doi:10.1007/978-1-62703-640-5_2 PubMed PMID: 23975817.
29. Woodward PW, Williams C, Sewing A, Benson N. Improving the design and analysis of high-throughput screening technology comparison experiments using statistical modeling. J Biomol Screen. 2006 Feb;11(1):5–12. doi:10.1177/1087057105280779 PubMed PMID: 16234338.
30. Camargo LM, Zhang XD, Loerch P, Caceres RM, Marine SD, Uva P, et al. Pathway-based analysis of genome-wide siRNA screens reveals the regulatory landscape of APP processing. PLoS One. 2015;10(2):e0115369. doi:10.1371/journal.pone.0115369 PubMed PMID: 25723573.
31. Langfelder P, Horvath S. WGCNA: an R package for weighted correlation network analysis. BMC Bioinformatics. 2008;9(1):559. doi:10.1186/1471-2105-9-559
32. Langfelder P, Zhang B, Horvath S. Defining clusters from a hierarchical cluster tree: the Dynamic Tree Cut package for R. Bioinformatics. 2008 Mar;24(5):719–20. doi:10.1093/bioinformatics/btm563 PubMed PMID: 18024473.
33. Saffari A, Brechmann B, Böger C, Saber WA, Jumo H, Whye D, et al. High-content screening identifies a small molecule that restores AP-4-dependent protein trafficking in neuronal models of AP-4-associated hereditary spastic paraplegia. Nat Commun. 2024 Jan;15(1):584. doi:10.1038/s41467-023-44264-1 PubMed PMID: 38233389.
34. Kannangara AR, Poole DM, McEwan CM, Youngs JC, Weerasekara VK, Thornock AM, et al. BioID reveals an ATG9A interaction with ATG13-ATG101 in the degradation of p62/SQSTM1-ubiquitin clusters. EMBO Rep. 2021 Oct;22(10):e51136. doi:10.15252/embr.202051136 PubMed PMID: 34369648.
35. Bock C, Datlinger P, Chardon F, Coelho MA, Dong MB, Lawson KA, et al. High-content CRISPR screening. Nature Reviews Methods Primers. 2022;2(1):8. doi:10.1038/s43586-021-00093-4
36. van der Knoop MM, Maroofian R, Fukata Y, van Ierland Y, Karimiani EG, Lehesjoki AE, et al. Biallelic ADAM22 pathogenic variants cause progressive encephalopathy and infantile-onset refractory epilepsy. Brain. 2022 Jul 1;145(7):2301–12. doi:10.1093/brain/awac116

37. Chen CA, Bosch DGM, Cho MT, Rosenfeld JA, Shinawi M, Lewis RA, et al. The expanding clinical phenotype of Bosch-Boonstra-Schaaf optic atrophy syndrome: 20 new cases and possible genotype-phenotype correlations. Genetics in Medicine. 2016 Nov 1;18(11):1143–50. doi:10.1038/gim.2016.18 PubMed PMID: 26986877.
38. Shaikh SS, Chen YC, Halsall SA, Nahorski MS, Omoto K, Young GT, et al. A Comprehensive Functional Analysis of NTRK1 Missense Mutations Causing Hereditary Sensory and Autonomic Neuropathy Type IV (HSAN IV). Hum Mutat. 2017 Jan 1;38(1):55–63. doi:https://doi.org/10.1002/humu.23123
39. Takashima H, Boerkoel CF, John J, Saifi GM, Salih MAM, Armstrong D, et al. Mutation of TDP1, encoding a topoisomerase I–dependent DNA damage repair enzyme, in spinocerebellar ataxia with axonal neuropathy. Nat Genet. 2002;32(2):267–72. doi:10.1038/ng987
40. Shen J, Yu WM, Brotto M, Scherman JA, Guo C, Stoddard C, et al. Deficiency of MIP/MTMR14 phosphatase induces a muscle disorder by disrupting Ca2+ homeostasis. Nat Cell Biol. 2009;11(6):769–76. doi:10.1038/ncb1884
41. Tosch V, Rohde HM, Tronchère H, Zanoteli E, Monroy N, Kretz C, et al. A novel PtdIns3P and PtdIns(3,5)P2 phosphatase with an inactivating variant in centronuclear myopathy. Hum Mol Genet. 2006 Nov 1;15(21):3098–106. doi:10.1093/hmg/ddl250
42. Vergne I, Roberts E, Elmaoued RA, Tosch V, Delgado MA, Proikas-Cezanne T, et al. Control of autophagy initiation by phosphoinositide 3-phosphatase jumpy. EMBO J. 2009;28(15):2244–58. doi:10.1038/emboj.2009.159
43. Kovács T, Billes V, Komlós M, Hotzi B, Manzéger A, Tarnóci A, et al. The small molecule AUTEN-99 (autophagy enhancer-99) prevents the progression of neurodegenerative symptoms. Sci Rep. 2017 Feb;7:42014. doi:10.1038/srep42014 PubMed PMID: 28205624.
44. Boada-Romero E, Letek M, Fleischer A, Pallauf K, Ramón-Barros C, Pimentel-Muiños FX. TMEM59 defines a novel ATG16L1-binding motif that promotes local activation of LC3. EMBO J. 2013;32(4):566–82. doi:10.1038/emboj.2013.8
45. Zheng N, Wang Z, Cao J, Li K, Xu H, Wang J, et al. TMEM59 deficiency activates chaperone-mediated autophagy and ameliorates disease-like pathologies in tauopathy model mice. Alzheimer's & Dementia. 2025 Jun 1;21(6):e70369. doi:https://doi.org/10.1002/alz.70369
46. Hetz C. The unfolded protein response: controlling cell fate decisions under ER stress and beyond. Nat Rev Mol Cell Biol. 2012;13(2):89–102. doi:10.1038/nrm3270
47. Nguyen LD, Nguyen LH, Dao DX, Hattori T, Takarada-Iemata M, Ishii H, et al. Impact of ATF6 deletion on the embryonic brain development. iScience. 2025 Jun 20;28(6). doi:10.1016/j.isci.2025.112569
48. Tan EHN, Tang BL. Rab7a and Mitophagosome Formation. Cells. 2019 Mar;8(3). doi:10.3390/cells8030224 PubMed PMID: 30857122.
49. Kakuta S, Yamaguchi J, Suzuki C, Sasaki M, Kazuno S, Uchiyama Y. Small GTPase Rab1B is associated with ATG9A vesicles and regulates autophagosome formation. FASEB J. 2017 Sep;31(9):3757–73. doi:10.1096/fj.201601052R PubMed PMID: 28522593.
50. Palmisano NJ, Rosario N, Wysocki M, Hong M, Grant B, Meléndez A. The recycling endosome protein RAB-10 promotes autophagic flux and localization of the

transmembrane protein ATG-9. Autophagy. 2017 Oct 3;13(10):1742–53. doi:10.1080/15548627.2017.1356976 PubMed PMID: 28872980.
51. Toh WH, Tan JZA, Zulkefli KL, Houghton FJ, Gleeson PA. Amyloid precursor protein traffics from the Golgi directly to early endosomes in an Arl5b- and AP4-dependent pathway. Traffic. 2017 Mar;18(3):159–75. doi:10.1111/tra.12465 PubMed PMID: 28000370.
52. Houghton FJ, Bellingham SA, Hill AF, Bourges D, Ang DKY, Gemetzis T, et al. Arl5b is a Golgi-localised small G protein involved in the regulation of retrograde transport. Exp Cell Res. 2012 Mar;318(5):464–77. doi:10.1016/j.yexcr.2011.12.023 PubMed PMID: 22245584.
53. Wu T, Shao Y, Li X, Wu T, Yu L, Liang J, et al. NR3C1/Glucocorticoid receptor activation promotes pancreatic β-cell autophagy overload in response to glucolipotoxicity. Autophagy. 2023;19(9):2538–57. doi:10.1080/15548627.2023.2200625 PubMed PMID: 37039556.
54. Müdsam C, Wollschläger P, Sauer N, Schneider S. Sorting of Arabidopsis NRAMP3 and NRAMP4 depends on adaptor protein complex AP4 and a dileucine-based motif. Traffic. 2018 Jul;19(7):503–21. doi:10.1111/tra.12567 PubMed PMID: 29573093.
55. Pertl-Obermeyer H, Wu XN, Schrodt J, Müdsam C, Obermeyer G, Schulze WX. Identification of Cargo for Adaptor Protein (AP) Complexes 3 and 4 by Sucrose Gradient Profiling. Mol Cell Proteomics. 2016 Sep;15(9):2877–89. doi:10.1074/mcp.M116.060129 PubMed PMID: 27371946.
56. Davies AK, Alecu JE, Ziegler M, Vasilopoulou CG, Merciai F, Jumo H, et al. AP-4-mediated axonal transport controls endocannabinoid production in neurons. Nat Commun. 2022 Feb;13(1):1058. doi:10.1038/s41467-022-28609-w PubMed PMID: 35217685.
57. Caracci MO, Pizarro H, Alarcón-Godoy C, Fuentealba LM, Farfán P, De Pace R, et al. The Reelin Receptor ApoER2 is a Cargo for the Adaptor Protein Complex AP-4: Implications for Hereditary Spastic Paraplegia. Prog Neurobiol. 2024 Jan;102575. doi:10.1016/j.pneurobio.2024.102575 PubMed PMID: 38281682.
58. Prat Castro S, Kudrina V, Jaślan D, Böck J, Scotto Rosato A, Grimm C. Neurodegenerative Lysosomal Storage Disorders: TPC2 Comes to the Rescue! Cells. 2022 Sep;11(18). doi:10.3390/cells11182807 PubMed PMID: 36139381.
59. Kubisch C, Schroeder BC, Friedrich T, Lütjohann B, El-Amraoui A, Marlin S, et al. KCNQ4, a novel potassium channel expressed in sensory outer hair cells, is mutated in dominant deafness. Cell. 1999 Feb;96(3):437–46. doi:10.1016/s0092-8674(00)80556-5 PubMed PMID: 10025409.
60. Worby CA, Dixon JE. Sorting out the cellular functions of sorting nexins. Nat Rev Mol Cell Biol. 2002 Dec 1;3(12):919–31. doi:10.1038/NRM974 PubMed PMID: 12461558.
61. Chen JH, Zhao Y, Khan RAW, Li ZQ, Zhou J, Shen JW, et al. SNX29, a new susceptibility gene shared with major mental disorders in Han Chinese population. World J Biol Psychiatry. 2021;22(7):526–34. doi:10.1080/15622975.2020.1845793 PubMed PMID: 33143498.
62. Mina-Osorio P. The moonlighting enzyme CD13: old and new functions to target. Trends Mol Med. 2008 Aug 1;14(8):361–71. doi:10.1016/j.molmed.2008.06.003
63. Lendeckel U, Karimi F, Al Abdulla R, Wolke C. The Role of the Ectopeptidase APN/CD13 in Cancer. Biomedicines. 2023;11(3). doi:10.3390/biomedicines11030724

64. Zhao Y, Wu H, Xing X, Ma Y, Ji S, Xu X, et al. CD13 Induces Autophagy to Promote Hepatocellular Carcinoma Cell Chemoresistance Through the P38/Hsp27/CREB/ATG7 Pathway. J Pharmacol Exp Ther. 2020 Sep 1;374(3):512–20. doi:10.1124/jpet.120.265637
65. Dwane S, Durack E, Kiely PA. Optimising parameters for the differentiation of SH-SY5Y cells to study cell adhesion and cell migration. BMC Res Notes. 2013 Sep;6:366. doi:10.1186/1756-0500-6-366 PubMed PMID: 24025096.
66. Wickham H, François R, Henry L, Müller K. dplyr: A Grammar of Data Manipulation [Internet]. 2022. Available from: https://CRAN.R-project.org/package=dplyr
67. Wickham H. ggplot2: Elegant Graphics for Data Analysis [Internet]. Springer-Verlag New York; 2016. Available from: https://ggplot2.tidyverse.org
68. Schauberger P, Walker A. openxlsx: Read, Write and Edit xlsx Files [Internet]. 2022. Available from: https://CRAN.R-project.org/package=openxlsx
69. Kassambara A. ggpubr: "ggplot2" Based Publication Ready Plots [Internet]. 2022. Available from: https://CRAN.R-project.org/package=ggpubr
70. Sievert C. Interactive Web-Based Data Visualization with R, plotly, and shiny [Internet]. Chapman and Hall/CRC; 2020. Available from: https://plotly-r.com
71. Slowikowski K. ggrepel: Automatically Position Non-Overlapping Text Labels with "ggplot2" [Internet]. 2022. Available from: https://CRAN.R-project.org/package=ggrepel
72. Attali D, Baker C. ggExtra: Add Marginal Histograms to "ggplot2", and More 'ggplot2' Enhancements [Internet]. 2022. Available from: https://CRAN.R-project.org/package=ggExtra
73. Firke S. janitor: Simple Tools for Examining and Cleaning Dirty Data [Internet]. 2023. Available from: https://CRAN.R-project.org/package=janitor
74. Navarro D. Learning statistics with R: A tutorial for psychology students and other beginners. (Version 0.6) [Internet]. Sydney, Australia; 2015. Available from: https://learningstatisticswithr.com
75. Wickham H, Girlich M. tidyr: Tidy Messy Data [Internet]. 2022. Available from: https://CRAN.R-project.org/package=tidyr
76. Müller K, Wickham H. tibble: Simple Data Frames [Internet]. 2022. Available from: https://CRAN.R-project.org/package=tibble
77. Gu Z, Eils R, Schlesner M. Complex heatmaps reveal patterns and correlations in multidimensional genomic data. Bioinformatics. 2016.
78. Gu Z. Complex Heatmap Visualization. iMeta. 2022.
79. Hothorn T, Bretz F, Westfall P. Simultaneous Inference in General Parametric Models. Biometrical Journal. 2008;50(3):346–63.
80. Ben-Shachar MS, Lüdecke D, Makowski D. effectsize: Estimation of Effect Size Indices and Standardized Parameters. J Open Source Softw. 2020;5(56):2815. doi:10.21105/joss.02815
81. Francois R, Hernangómez D. bibtex: Bibtex Parser [Internet]. 2023. Available from: https://CRAN.R-project.org/package=bibtex
82. Soudy M, Anwar AM, Ahmed EA, Osama A, Ezzeldin S, Mahgou S, et al. UniprotR: Retrieving and visualizing protein sequence and functional information from Universal Protein Resource (UniProt knowledgebase). J Proteomics. 2020;213:103613. doi:10.1016/j.jprot.2019.103613

83. Langfelder P, Zhang B, with contributions from Steve Horvath. dynamicTreeCut: Methods for Detection of Clusters in Hierarchical Clustering Dendrograms [Internet]. 2016. Available from: https://CRAN.R-project.org/package=dynamicTreeCut
84. Xu S, Chen M, Feng T, Zhan L, Zhou L, Yu G. Use ggbreak to effectively utilize plotting space to deal with large datasets and outliers. Front Genet. 2021;12:774846. doi:10.3389/fgene.2021.774846
85. Morales C, Lou J, Zhang J, Lvy Y, Jin Z. gggap: Streamlined Creation of Segments on the Y-Axis of 'ggplot2' Plots [Internet]. 2020. Available from: https://CRAN.R-project.org/package=gggap
86. Solymos P, Zawadzki Z. pbapply: Adding Progress Bar to "*apply" Functions [Internet]. 2023. Available from: https://CRAN.R-project.org/package=pbapply
87. Maechler M, Rousseeuw P, Struyf A, Hubert M, Hornik K. cluster: Cluster Analysis Basics and Extensions [Internet]. 2022. Available from: https://CRAN.R-project.org/package=cluster
88. Wickham H, Henry L. purrr: Functional Programming Tools [Internet]. 2023. Available from: https://CRAN.R-project.org/package=purrr
89. Langfelder P, Horvath S. moduleColor: Basic Module Functions [Internet]. 2022. Available from: https://CRAN.R-project.org/package=moduleColor
90. Wright K. pals: Color Palettes, Colormaps, and Tools to Evaluate Them [Internet]. 2021. Available from: https://CRAN.R-project.org/package=pals
91. Harrell Jr FE. Hmisc: Harrell Miscellaneous [Internet]. 2022. Available from: https://CRAN.R-project.org/package=Hmisc
92. Durinck S, Moreau Y, Kasprzyk A, Davis S, De Moor B, Brazma A, et al. BioMart and Bioconductor: a powerful link between biological databases and microarray data analysis. Bioinformatics. 2005;21:3439–40.
93. Durinck S, Spellman PT, Birney E, Huber W. Mapping identifiers for the integration of genomic datasets with the R/Bioconductor package biomaRt. Nat Protoc. 2009;4:1184–91.
94. Wickham H, Seidel D. scales: Scale Functions for Visualization [Internet]. 2022. Available from: https://CRAN.R-project.org/package=scales
95. Neuwirth E. RColorBrewer: ColorBrewer Palettes [Internet]. 2022. Available from: https://CRAN.R-project.org/package=RColorBrewer
96. Gu Z, Gu L, Eils R, Schlesner M, Brors B. circlize implements and enhances circular visualization in R. Bioinformatics. 2014;30(19):2811–2.
97. Ordak M. Multiple comparisons and effect size: Statistical recommendations for authors planning to submit an article to Allergy. Allergy. Denmark; 2023. p. 1145–7. doi:10.1111/all.15700 PubMed PMID: 36883352.

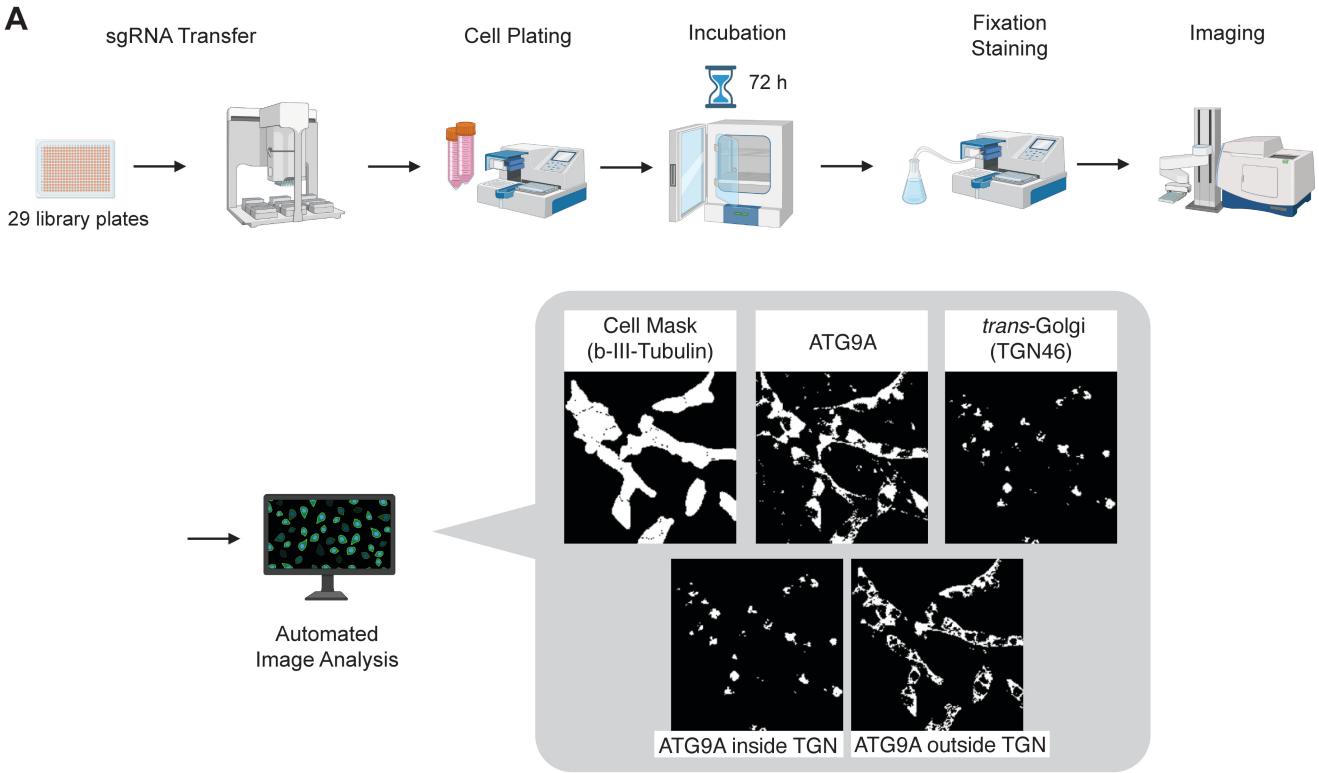
A
sgRNA Transfer
Cell Plating
Incubation
72 h
Fixation
Staining
Imaging
29 library plates
Automated
Image Analysis
Cell Mask
(b-III-Tubulin)
ATG9A
trans-Golgi
(TGN46)
ATG9A inside TGN
ATG9A outside TGN

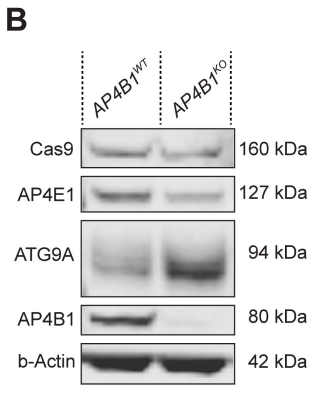
B
AP4B1WT
AP4B1KO
Cas9
160 kDa
AP4E1
127 kDa
ATG9A
94 kDa
AP4B1
80 kDa
b-Actin
42 kDa

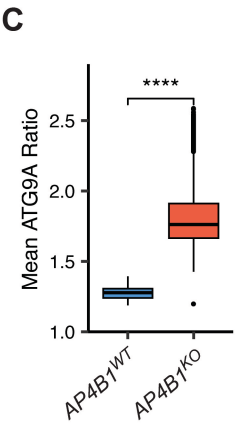
C
****
Mean ATG9A Ratio
2.5
2.0
1.5
1.0
AP4B1WT
AP4B1KO

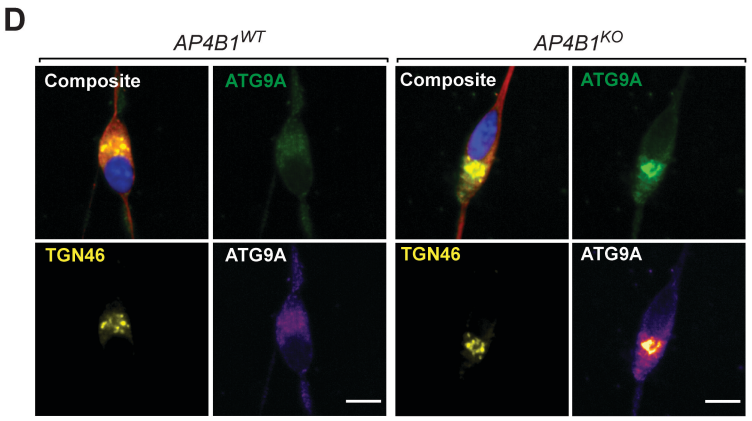
D
AP4B1WT
AP4B1KO
Composite
ATG9A
TGN46

Figure 1: Establishment of a High-Content CRISPR/Cas9 Loss-Of-Function Screening Platform

A) Experimental workflow for CRISPR/Cas9 screen. Control and library sgRNAs were transferred into 384-well plates preloaded with Lipofectamine™ RNAiMAX. Differentiated Cas9 expressing SH-SY5Y cells were plated on top and incubated with sgRNAs for 72 hours. Cells were subsequently fixed and stained with Hoechst 33258 (nuclear marker), β-Tubulin III (cytoplasmic marker), TGN46 (*trans*-Golgi network marker), and ATG9A (ATG9A compartment marker). Plates were imaged using an automated high-content imaging platform (Molecular Devices ImageXpress Micro Confocal Laser System and PAA GX™ robot arm), and images were analyzed using an automated pipeline in MetaXpress to segment cells and calculate the proportion of ATG9A signal overlapping with the TGN. This figure was partially created in BioRender. Kim, H. (2026) https://BioRender.com/jrlyt8e. Cellular compartment masks derived from MetaXpress.

B) Western blot analysis of whole-cell lysates from differentiated *AP4B1*^{KO} and *AP4B1*^{WT} SH-SY5Y cells. *AP4B1*^{KO} cells showed loss of AP4B1 protein and reduced levels of AP4E1, indicating successful *AP4B1* knockout and decreased AP-4 complex formation. ATG9A levels were increased in *AP4B1*^{KO} cells. Both cell lines demonstrated stable expression of Cas9.

C) ATG9A ratio of untransfected *AP4B1*^{KO} and *AP4B1*^{WT} cells, based on all wells from the primary screen. *AP4B1*^{KO} cells showed a significant increase in the ATG9A ratio, consistent with accumulation of ATG9A in the TGN. Statistical analysis: Two-sided Student's t-test, $p < 0.001$ (***), Cohen's $d \approx 2.74$.

D) Representative images of *AP4B1*^{KO} and *AP4B1*^{WT} SH-SY5Y cells stained with

antibodies against ATG9A and TGN46. *AP4B1*^{KO} cells exhibited perinuclear accumulation of ATG9A overlapping with the TGN. Pseudocolored images depict grayscale intensity. Scale bar = 10 μm.

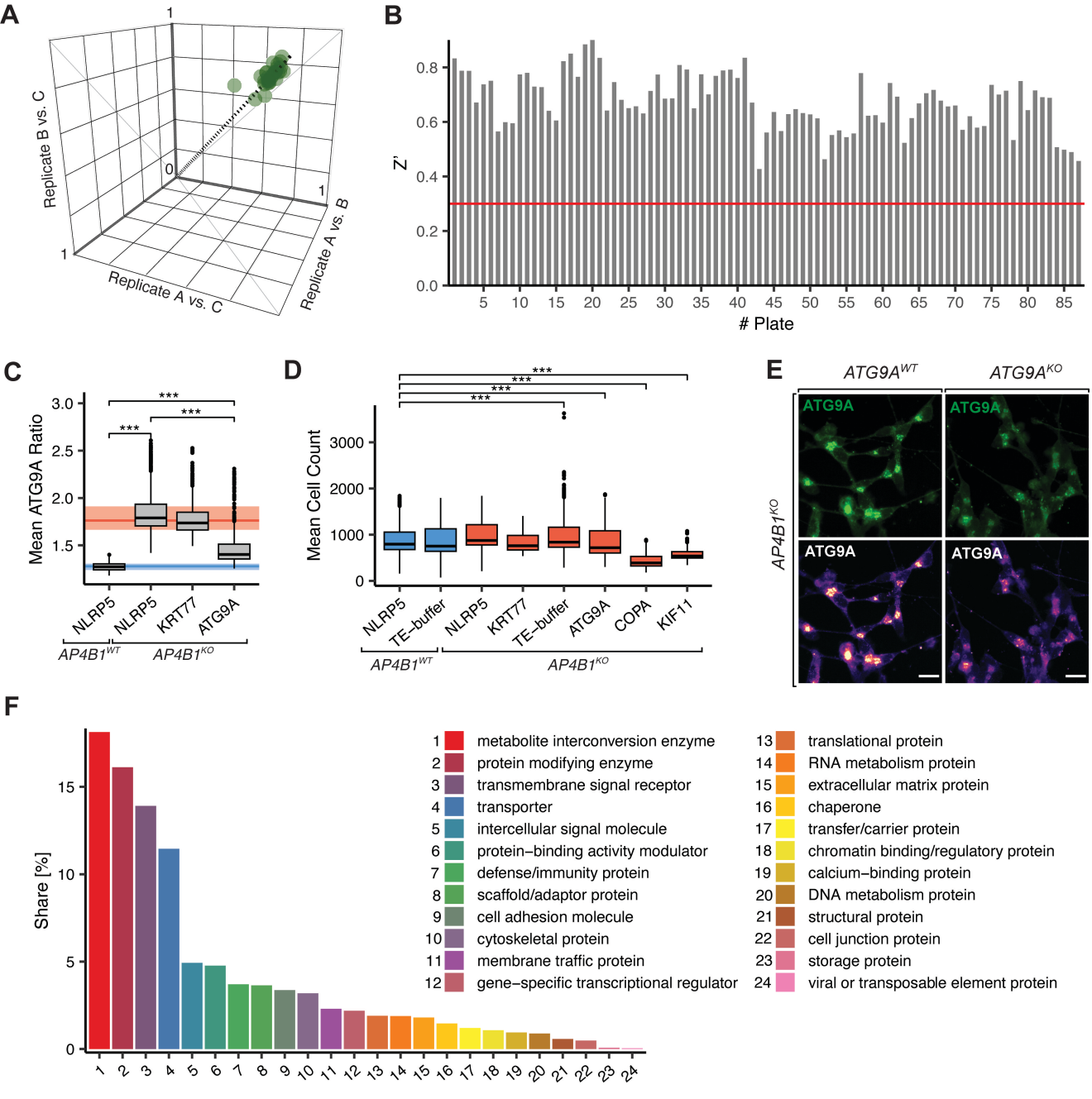
A
Replicate B vs. C
Replicate A vs. C
Replicate A vs. B
B
Z'
Plate
C
Mean ATG9A Ratio
NLRP5
NLRP5
KRT77
ATG9A
AP4B1WT
AP4B1KO
D
Mean Cell Count
NLRP5
TE−buffer
NLRP5
KRT77
TE−buffer
ATG9A
COPA
KIF11
AP4B1WT
AP4B1KO
E
ATG9AWT
ATG9AKO
AP4B1KO
ATG9A
F
Share [%]
1 metabolite interconversion enzyme
2 protein modifying enzyme
3 transmembrane signal receptor
4 transporter
5 intercellular signal molecule
6 protein−binding activity modulator
7 defense/immunity protein
8 scaffold/adaptor protein
9 cell adhesion molecule
10 cytoskeletal protein
11 membrane traffic protein
12 gene−specific transcriptional regulator
13 translational protein
14 RNA metabolism protein
15 extracellular matrix protein
16 chaperone
17 transfer/carrier protein
18 chromatin binding/regulatory protein
19 calcium−binding protein
20 DNA metabolism protein
21 structural protein
22 cell junction protein
23 storage protein
24 viral or transposable element protein

Figure 2: Quality Metrics for High-Throughput Screen and sgRNA Library

A) Pearson correlation coefficients between replicates across all plates in the primary screen. High correlation between replicates demonstrated low interplate variability. Mean Pearson correlation coefficient: 0.907 ± 0.035.

B) Z' robust for all 87 screened plates confirmed reliable assay performance. Horizontal line indicates predefined quality control threshold (Z' > 0.3).

C) ATG9A Ratio for *AP4B1*^{KO} and *AP4B1*^{WT} cells transfected with sgRNAs targeting non-essential genes (*NLRP5* and *KRT77*), *ATG9A*, and essential genes (*COPA* and *KIF11*). Red lines represent the ATG9A ratio ± SD for untransfected *AP4B1*^{KO} cells (negative control), and blue lines represent the same for *AP4B1*^{WT} cells (positive control). Statistical analysis: One-way ANOVA, $F(5) = 1908$, $p < 0.001$, $\eta^2 = 0.58$. Tukey HSD post hoc test revealed significant differences between groups $p < 0.001$ (***).

D) Mean cell counts for *AP4B1*^{KO} (red) and *AP4B1*^{WT} (blue) cells, including untransfected controls (TE-buffer) and cells transfected with sgRNAs targeting non-essential (*NLRP5*, *KRT77*) and essential (*COPA*, *KIF11*) genes, as well as ATG9A. Transfection with sgRNAs targeting essential genes significantly reduced cell counts, confirming efficient transfection and gene knockout. Statistical analysis: One-way ANOVA, $F(7) = 163$, $p < 0.001$, $\eta^2 = 0.13$. Dunnett's post hoc test identified significant group differences $p < 0.01$ (**) and $p < 0.001$ (***).

E) Representative images of *AP4B1*^{KO}/*ATG9A*^{WT} (top panel) and *AP4B1*^{KO}/*ATG9A*^{KO} (bottom panel) SH-SY5Y cells stained for ATG9A and TGN46. Pseudocolored images depict grayscale intensity. Scale bar = 20 µm.

F) Frequency of Panther GO terms associated with genes in the ‘Synthego Human Druggable Genome’ library.

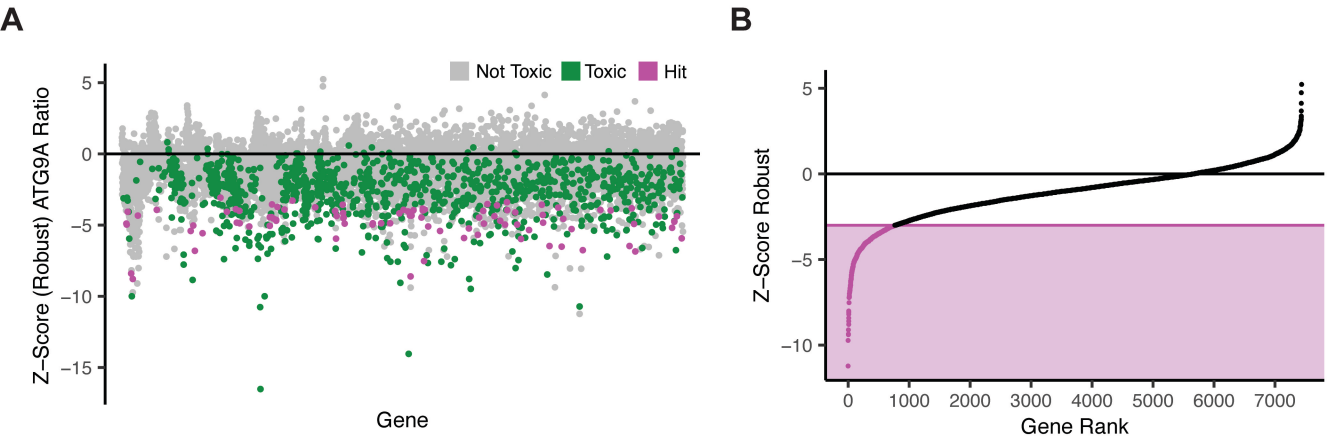
A
Not Toxic
Toxic
Hit
Z−Score (Robust) ATG9A Ratio
5
0
−5
−10
−15
Gene
B
Z−Score Robust
5
0
−5
−10
0
1000
2000
3000
4000
5000
6000
7000
Gene Rank

Figure 3. Primary Screen Identifies Modulators of ATG9A Trafficking

A) Distribution of robust z-scores from the primary screen. Genes are categorized as toxic (z-score robust for cell count < -3 in at least two replicates), not-toxic, or hits (not-toxic & z-score robust for ATG9A ratio < -3 in all replicates). A total of 92 genes were identified as hits, while 1,041 genes were classified as toxic.

B) Ranked distribution of robust z-scores for all screened genes. Genes with a mean robust z-score < -3 across all replicates are highlighted. While only 92 genes met the stringent cut-off criteria of robust z-scores < -3 in all replicates and were classified as hits, 764 genes exhibited a mean robust z-score < -3 across all replicates, indicating a strong but less reproducible impact on ATG9A trafficking.

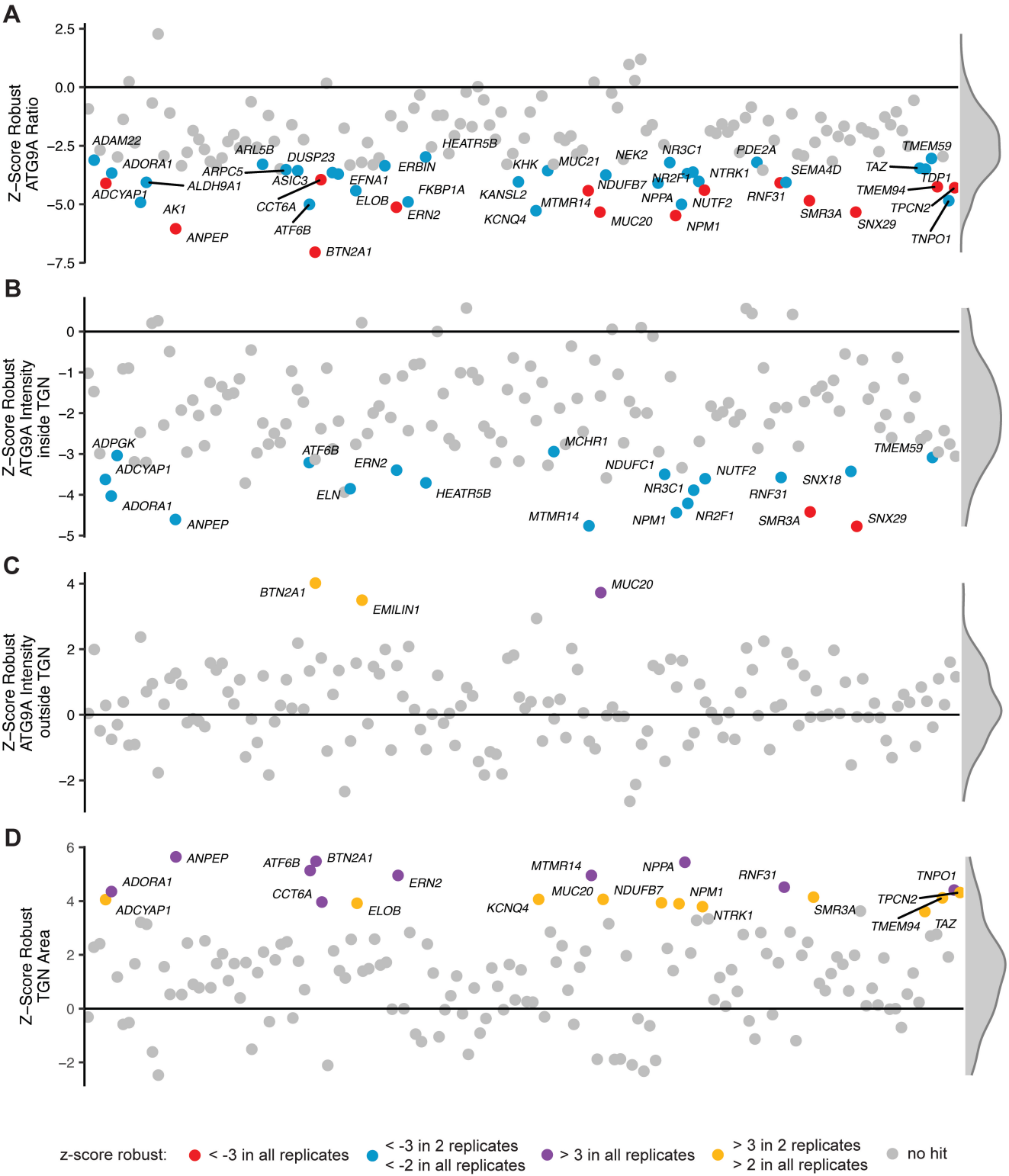
A
Z−Score Robust ATG9A Ratio
2.5
0.0
−2.5
−5.0
−7.5
ADAM22
ADORA1
ADCYAP1
ALDH9A1
AK1
ANPEP
ARL5B
ARPC5
DUSP23
ASIC3
CCT6A
ATF6B
BTN2A1
EFNA1
ELOB
ERBIN
FKBP1A
ERN2
HEATR5B
KANSL2
KCNQ4
KHK
MUC21
MTMR14
NEK2
NDUFB7
MUC20
NR3C1
NR2F1
NPPA
NUTF2
NPM1
PDE2A
NTRK1
RNF31
SEMA4D
SMR3A
TAZ
TMEM59
TDP1
TMEM94
TPCN2
SNX29
TNPO1
B
Z−Score Robust ATG9A Intensity inside TGN
0
−1
−2
−3
−4
−5
ADPGK
ADCYAP1
ADORA1
ANPEP
ATF6B
ELN
ERN2
HEATR5B
MCHR1
MTMR14
NDUFC1
NR3C1
NPM1
NR2F1
NUTF2
RNF31
SNX18
SMR3A
TMEM59
SNX29
C
Z−Score Robust ATG9A Intensity outside TGN
4
2
0
−2
BTN2A1
EMILIN1
MUC20
D
Z−Score Robust TGN Area
6
4
2
0
−2
ANPEP
ADORA1
ADCYAP1
ATF6B
BTN2A1
CCT6A
ELOB
ERN2
MTMR14
KCNQ4
MUC20
NPPA
NDUFB7
NPM1
NTRK1
RNF31
SMR3A
TNPO1
TPCN2
TMEM94
TAZ
z-score robust:
< -3 in all replicates
< -3 in 2 replicates
< -2 in all replicates
> 3 in all replicates
> 3 in 2 replicates
> 2 in all replicates
no hit

Figure 4: Secondary Screen Validates Modulators of ATG9A Trafficking

A) Results of the secondary screen demonstrating robust z-scores for the ATG9A ratio. A total of 14 genes were confirmed as hits (robust z-scores < -3 in all replicates), additionally 30 genes met the less stringent criteria of robust z-scores < -3 in two replicates and < -2 in all replicates.

B) Robust z-scores for ATG9A intensity inside the TGN in the secondary screen. Most hits reduced the ATG9A ratio by decreasing ATG9A intensity within the TGN.

C) Robust z-scores for ATG9A intensity outside the TGN. Most genes had minimal impact on ATG9A intensity outside the TGN.

D) Robust z-scores for TGN area. Several genes affected TGN morphology, as evidenced by an increase in TGN area, potentially indicating early toxicity or structural reorganization.

Density distribution of robust z-scores displayed on the right in *C) – F)*.

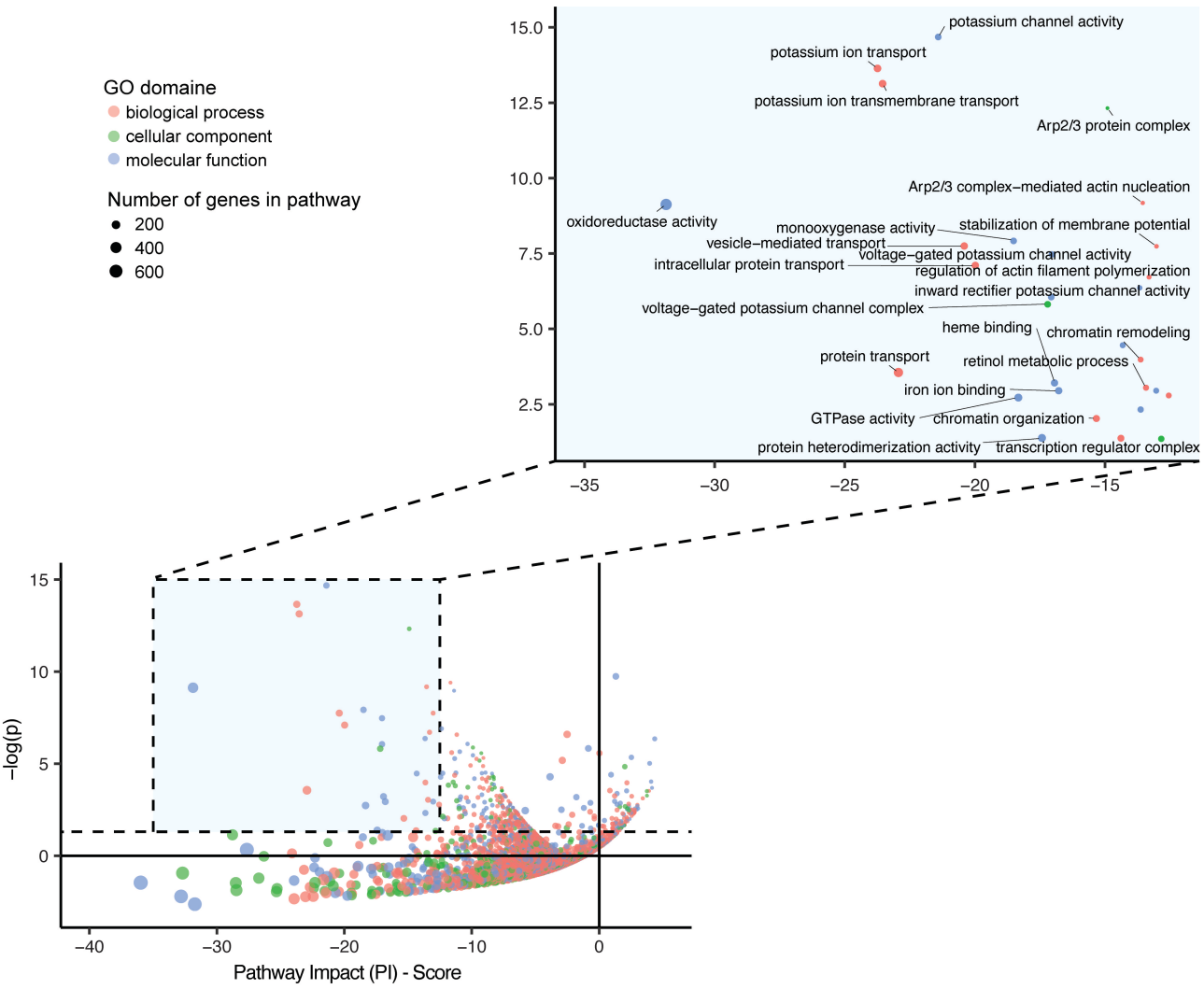
GO domaine
biological process
cellular component
molecular function
Number of genes in pathway
200
400
600
potassium channel activity
potassium ion transport
potassium ion transmembrane transport
Arp2/3 protein complex
Arp2/3 complex−mediated actin nucleation
oxidoreductase activity
monooxygenase activity
stabilization of membrane potential
vesicle−mediated transport
voltage−gated potassium channel activity
intracellular protein transport
regulation of actin filament polymerization
inward rectifier potassium channel activity
voltage−gated potassium channel complex
heme binding
chromatin remodeling
protein transport
retinol metabolic process
iron ion binding
GTPase activity
chromatin organization
protein heterodimerization activity
transcription regulator complex
15.0
12.5
10.0
7.5
5.0
2.5
−35
−30
−25
−20
−15
15
10
5
0
−log(p)
−40
−30
−20
−10
0
Pathway Impact (PI) - Score

Figure 5: Pathway Analysis Reveals the Modulatory Landscape of ATG9A Trafficking

Pathway analysis of primary screen results. Each dot represents a GO term. Pathway Impact (PI) score reflects the cumulative robust z-score of all genes associated with the respective GO term adjusted for its size. Dot size corresponds to number of genes linked to the GO term; color indicates gene ontology branch. Detailed view of significant pathways with PI scores between -35 and -12.5 on the right, selected pathways labeled for clarity.

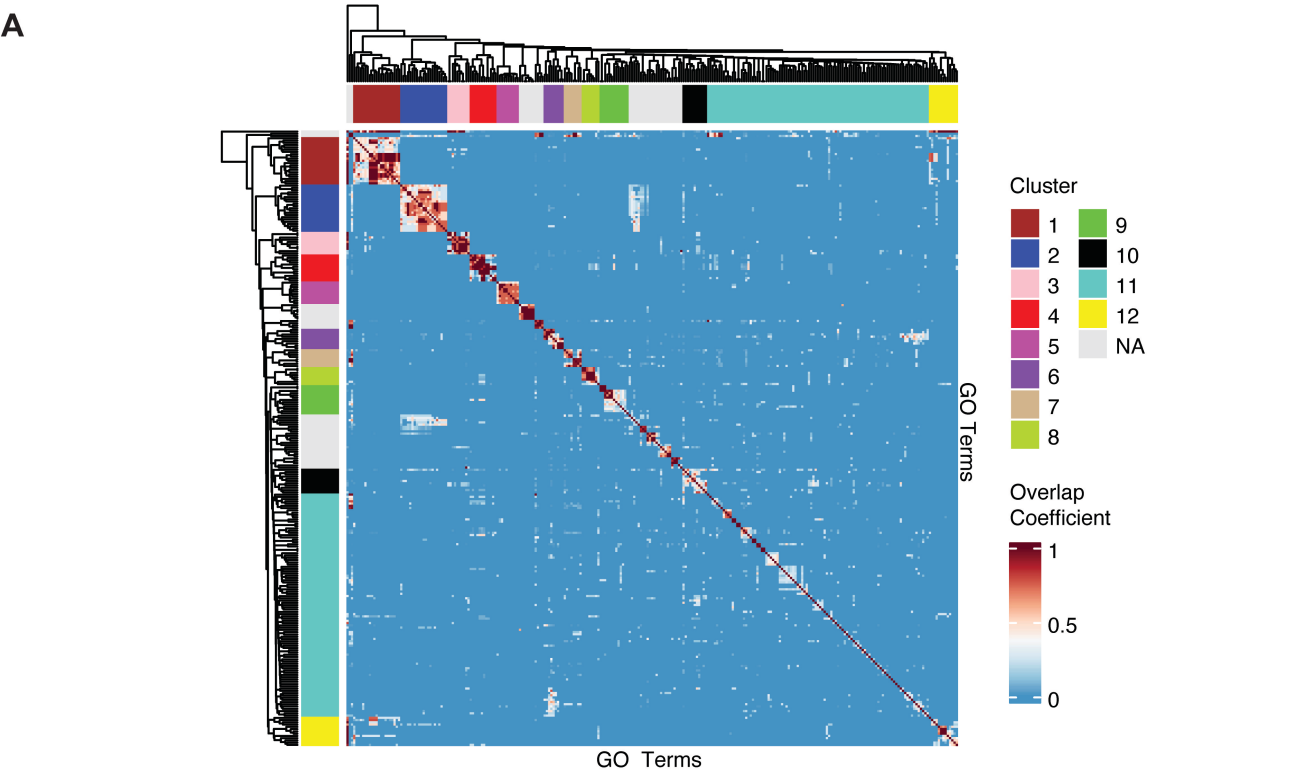
A
Cluster
1
2
3
4
5
6
7
8
9
10
11
12
NA
Overlap
Coefficient
1
0.5
0
GO Terms
GO Terms

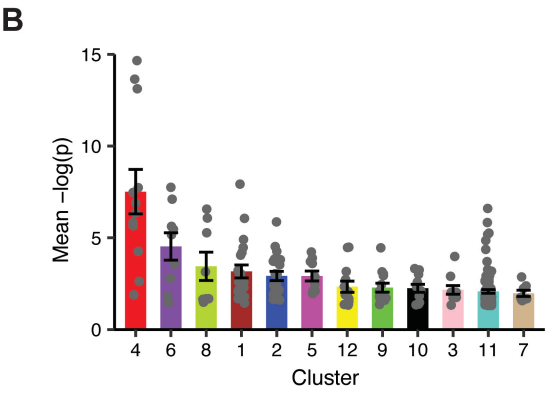
B
Mean −log(p)
15
10
5
0
4
6
8
1
2
5
12
9
10
3
11
7
Cluster

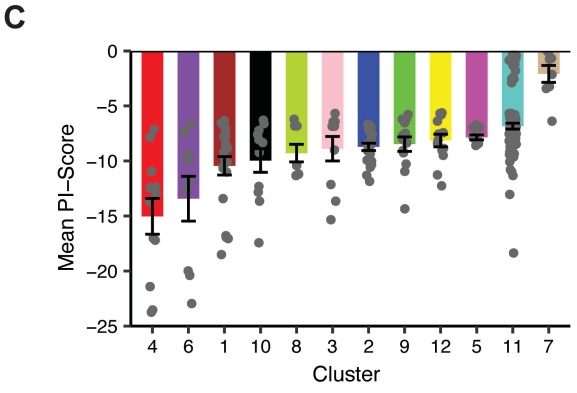
C
Mean PI−Score
0
−5
−10
−15
−20
−25
4
6
1
10
8
3
2
9
12
5
11
7
Cluster

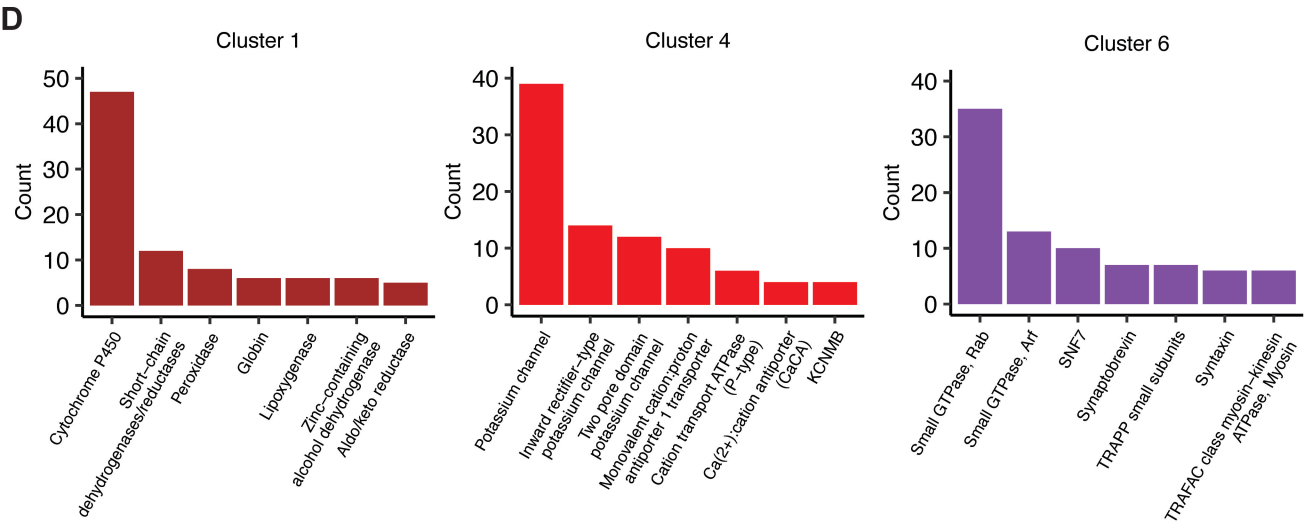
D
Cluster 1
Count
50
40
30
20
10
0
Cytochrome P450
Short−chain dehydrogenases/reductases
Peroxidase
Globin
Lipoxygenase
Zinc−containing alcohol dehydrogenase
Aldo/keto reductase
Cluster 4
Count
40
30
20
10
0
Potassium channel
Inward rectifier−type potassium channel
Two pore domain potassium channel
Monovalent cation:proton antiporter 1 transporter
Cation transport ATPase (P−type)
Ca(2+)-cation antiporter (CaCA)
KCNMB
Cluster 6
Count
40
30
20
10
0
Small GTPase, Rab
Small GTPase, Arf
SNF7
Synaptobrevin
TRAPP small subunits
Syntaxin
TRAFAC class myosin−kinesin ATPase, Myosin

Figure 6: Pathway Clustering Defines Regulatory Pathways of ATG9A Trafficking

A) Heatmap of genetic overlap between GO terms sorted by average linkage clustering. Overlap coefficients range from 0 (no genetic overlap) to 1 (complete genetic overlap of the smaller GO term with the larger GO term). Color bars on heatmap edges indicate clusters identified with the Dynamic Tree Cut algorithm.

B) Mean p-values and standard deviations across pathways associated with identified clusters, highlighting their statistical significance.

C) Mean PI scores and standard deviations across pathways associated with identified clusters, indicating cumulative impact of genes on ATG9A trafficking within each cluster.

D) Protein families and number of proteins from each family associated with top three clusters: Cluster 1 (oxidative degradation, 192 proteins), cluster 4 (potassium channel activity, 133 proteins), and cluster 6 (vesicular transport, 308 proteins).

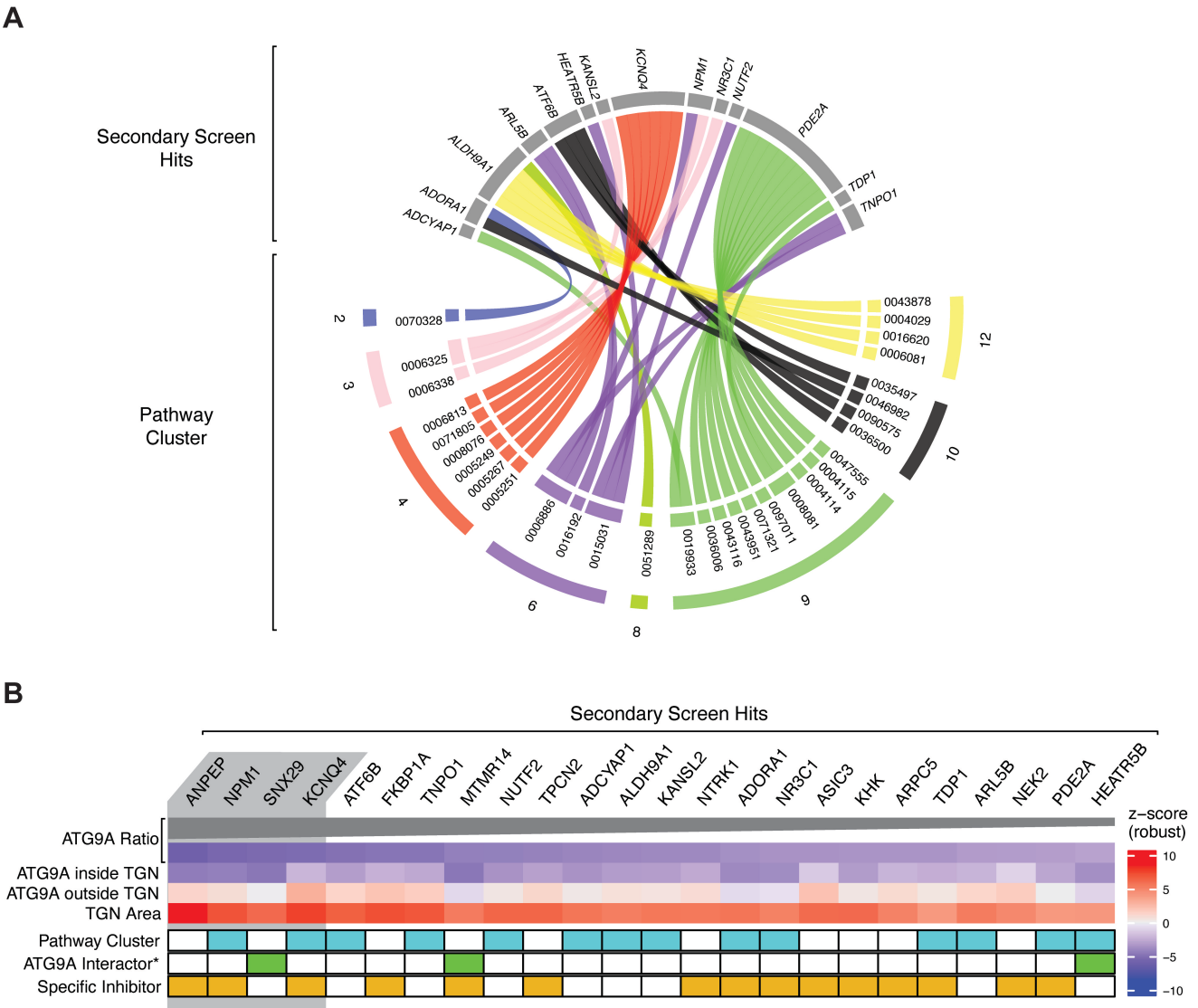
A
Secondary Screen Hits
Pathway Cluster
KCNQ4
NPM1
NR3C1
NUTF2
PDE2A
TDP1
TNPO1
ADCYAP1
ADORA1
ALDH9A1
ARL5B
ATF6B
HEATR5B
KANSL2
0070328
0006325
0006338
0006813
0071805
0008076
0005249
0005267
0005251
0006886
0016192
0015031
0051289
0019933
0036006
0043951
0043116
0071321
0097011
0008081
0004114
0004115
0047555
0036500
0090575
0046982
0035497
0006081
0016620
0004029
0043878
2
3
4
6
8
9
10
12
B
Secondary Screen Hits
ANPEP
NPM1
SNX29
KCNQ4
ATF6B
FKBP1A
TNPO1
MTMR14
NUTF2
TPCN2
ADCYAP1
ALDH9A1
KANSL2
NTRK1
ADORA1
NR3C1
ASIC3
KHK
ARPC5
TDP1
ARL5B
NEK2
PDE2A
HEATR5B
ATG9A Ratio
ATG9A inside TGN
ATG9A outside TGN
TGN Area
Pathway Cluster
ATG9A Interactor*
Specific Inhibitor
z−score
(robust)
10
5
0
−5
−10

Figure 7: Selection of Relevant Genes for Follow-Up

A) Secondary screen hits matched to significantly affected pathways and respective clusters (*Supplementary File 5*), identifying key modulators of ATG9A trafficking in AP4-deficient cells.

B) Selected secondary screen hits ranked by mean ATG9A ratio reduction across all replicates in the secondary screen and meeting at least one of the following criteria: 1. Association with a pathway cluster, 2. identification as an ATG9A interactor by BioID (34), and 3. availability of a specific small molecule inhibitor. Heatmap summarizes secondary screen results.

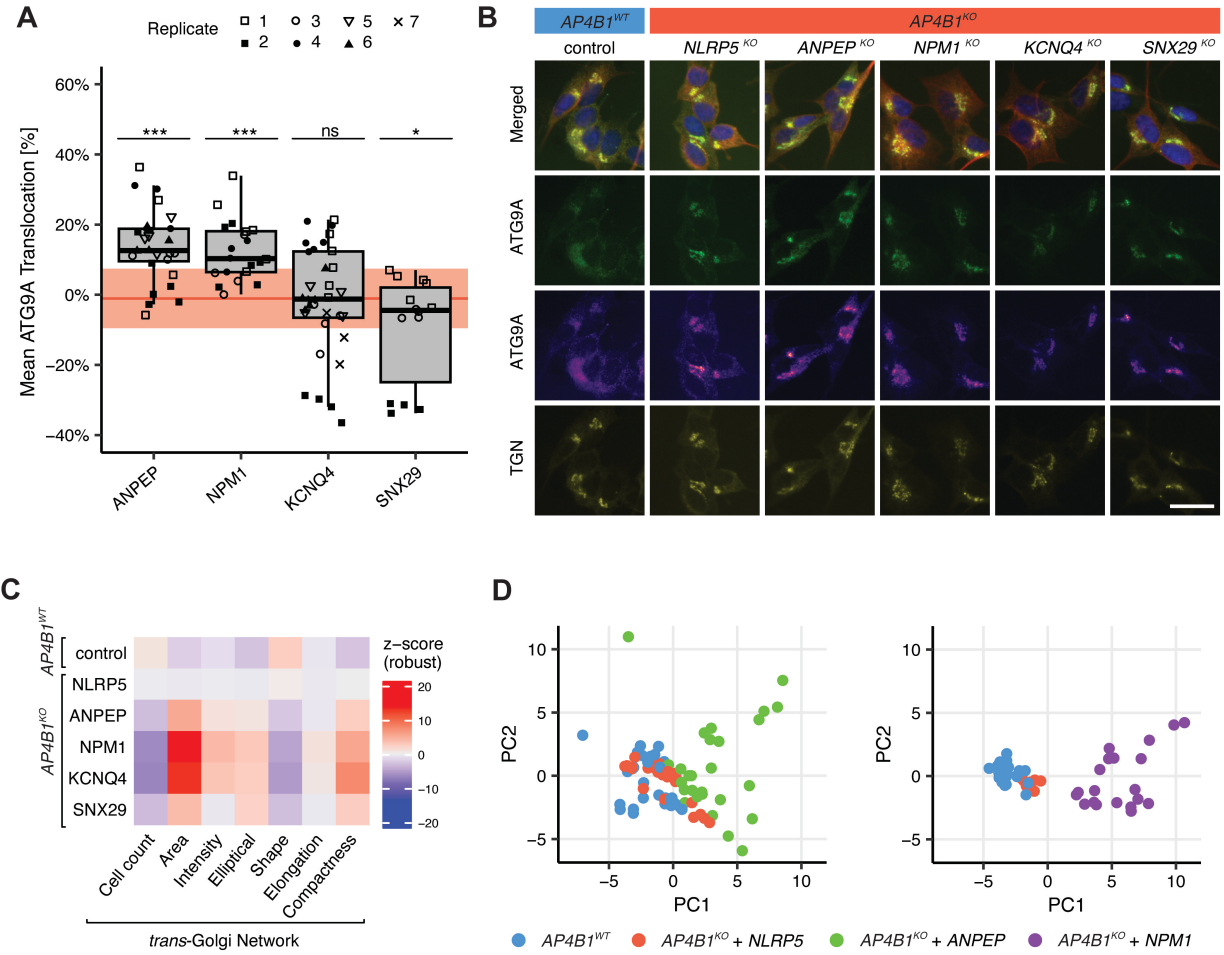
A
Replicate
1
2
3
4
5
6
7
Mean ATG9A Translocation [%]
60%
40%
20%
0%
−20%
−40%
***
***
ns
*
ANPEP
NPM1
KCNQ4
SNX29
B
AP4B1WT
AP4B1KO
control
NLRP5 KO
ANPEP KO
NPM1 KO
KCNQ4 KO
SNX29 KO
Merged
ATG9A
ATG9A
TGN
C
AP4B1WT
AP4B1KO
control
NLRP5
ANPEP
NPM1
KCNQ4
SNX29
z−score
(robust)
20
10
0
−10
−20
Cell count
Area
Intensity
Elliptical
Shape
Elongation
Compactness
trans-Golgi Network
D
PC2
PC1
10
5
0
−5
−5
0
5
10
AP4B1WT
AP4B1KO + NLRP5
AP4B1KO + ANPEP
AP4B1KO + NPM1

Figure 8: Validation of Hits Affecting ATG9A Translocation

A) Mean ATG9A translocation across up to seven independent biological replicates after knockout of the top four genes (*ANPEP*, *NPM1*, *KCNQ4*, and *SNX29*) compared to knockout of the non-essential gene *NLRP5* (red line and area indicate mean ± SD) in AP4B1^{KO} cells. Statistical analysis using one-way ANOVA revealed a significant effect of gene knockout on ATG9A translocation ($F(5) = 20.48$, $p < 0.001$, $\eta^2 = 0.27$). Dunnett's post hoc test indicated significant differences in ATG9A translocation for *AP4B1^{KO}* + *ANPEP*, *AP4B1^{KO}* + *NPM1*, and *AP4B1^{KO}* + *SNX29* compared to *AP4B1^{KO}* + *NLRP5*. No significant differences were observed between *AP4B1^{KO}* + *KCNQ4* and *AP4B1^{KO}* + *NLRP5*. Significance level denoted as $p > 0.05$ (ns), $p < 0.05$ (*) and $p < 0.001$ (***).

B) Representative fluorescence images of *AP4B1^{WT}* and *AP4B1^{KO}* cells following knockout of *NLRP5* (negative control), *ANPEP*, *KCNQ4*, and *SNX29*. Images highlight differences in ATG9A localization and TGN morphology. Scale bar = 20 µm.

C) Heatmap illustrating mean z-scores for cell count and six selected parameters describing TGN morphology.

D) Dimensionality reduction of 25 ATG9A independent cell morphology parameters by principal component analysis (PCA) demonstrated little to no morphological difference between *AP4B1^{WT}* and *AP4B1^{KO}* cells. Knockout of *NPM1* resulted in a pronounced deviation from controls, while knockout of *ANPEP* caused substantially less morphological changes.

TABLES

Table 1: Pathway Clusters Identified by Average-Linkage Hierarchical Clustering Based On Genetic Overlap Between Significantly Affected Pathways

Cluster	# GO Terms	# Genes	Description	Example
1	21	192	Oxidative Degradation	caffeine oxidase activity, cellular aromatic compound metabolic process, demethylase activity, aflatoxin metabolic process, estrogen 2-hydroxylase activity
2	21	71	Lipid Metabolism	intermediate-density lipoprotein particle, lipase inhibitor activity, negative regulation of cholesterol transport, negative regulation of lipid metabolic process, negative regulation of receptor-mediated endocytosis
3	10	128	Histone H3 Demethylation	histone H3-K4 demethylation, histone H3-methyl-lysine-4 demethylase activity, histone H3-tri/dimethyl-lysine-9 demethylase activity, negative regulation of histone H3-K9 trimethylation, histone H3-K9 demethylation
4	12	133	Potassium Channel Activity	small conductance calcium-activated potassium channel activity, calcium-activated potassium channel activity, potassium ion export across plasma membrane, potassium ion leak

				channel activity, stabilization of membrane potential
5	10	21	Splicesosom	methylosome, precatalytic spliceosome, SMN-Sm protein complex, U1 snRNP, U5 snRNP
6	9	308	Vesicular Transport	clathrin adaptor complex, clathrin adaptor activity, TRAPPIII protein complex, TRAPP complex, Golgi vesicle transport
7	8	203	Chemotaxis	C-C chemokine binding, C-C chemokine receptor activity, monocyte chemotaxis, chemokine activity, cell chemotaxis
8	8	48	Water/Urea Transport	cellular water homeostasis, glycerol channel activity, urea transmembrane transport, urea transmembrane transporter activity, glycerol transport
9	13	83	Signal Transduction	cellular response to cGMP, sphingomyelin catabolic process, sphingomyelin phosphodiesterase activity, Tie signaling pathway, cellular response to macrophage colony-stimulating factor stimulus
10	11	239	Cellular Stress Response	aryl hydrocarbon receptor complex, ATF6-mediated unfolded protein response, cellular response to leucine starvation, leucine zipper domain binding, regulation of transcription from RNA polymerase

				II promoter in response to oxidative stress
11	99	1337	Miscellaneous	1-phosphatidylinositol binding, activation of phospholipase D activity, alpha-2A adrenergic receptor binding, androgen binding, arginine biosynthetic process
12	13	64	Sterol Metabolism	9-cis-retinoic acid biosynthetic process, alcohol dehydrogenase (NADP+) activity, C21-steroid hormone metabolic process, vitamin D catabolic process, cholesterol catabolic process

SUPPLEMENTAL MATERIAL

Supplementary Tables

Supplementary Table 1: Key Resources

Supplementary Figures

Supplementary Figure 1: Uncut Western Blots (Figure 1B)

Supplementary Figure 2: Primary Screen Plate Design and Quality Control Metrics

Supplementary Figure 3: Overview of Primary and Secondary Screens and Comparison of Hit Genes

Supplementary Figure 4: Validation Experiments Plate Design and Quality Control Metrics

Supplementary Figure 5: Validation of knockout efficiency for selected hit genes.

Supplementary Files:

Supporting Data Values File

Supplementary File 1:	Complete dataset for the primary screen
Supplementary File 2:	Complete dataset for the secondary screen
Supplementary File 3:	List of GO terms derived from Ensemble (accessed: 09/19/2022)
Supplementary File 4:	Complete dataset of significant pathways
Supplementary File 5:	Significant pathways in relevant pathway clusters associated with secondary screen hits
Supplementary File 6:	Raw data for Figures 8 *A*, *C* and *D*